Reliability of micritic carbonates in recording well-preserved isotopic composition and implications for paleoelevation estimates in central Tibet

Lin Li, Jay Quade, Carmala Garzione, William F. Defliese, Peter DeCelles, Paul Kapp

PII: S0016-7037(24)00179-0

DOI: https://doi.org/10.1016/j.gca.2024.04.009

Reference: GCA 13381

To appear in: Geochimica et Cosmochimica Acta

Received Date: 13 September 2023

Accepted Date: 5 April 2024



Please cite this article as: Li, L., Quade, J., Garzione, C., Defliese, W.F., DeCelles, P., Kapp, P., Reliability of micritic carbonates in recording well-preserved isotopic composition and implications for paleoelevation estimates in central Tibet, *Geochimica et Cosmochimica Acta* (2024), doi: https://doi.org/10.1016/j.gca. 2024.04.009

This is a PDF file of an article that has undergone enhancements after acceptance, such as the addition of a cover page and metadata, and formatting for readability, but it is not yet the definitive version of record. This version will undergo additional copyediting, typesetting and review before it is published in its final form, but we are providing this version to give early visibility of the article. Please note that, during the production process, errors may be discovered which could affect the content, and all legal disclaimers that apply to the journal pertain.

© 2024 Published by Elsevier Ltd.

- 1 Reliability of micritic carbonates in recording well-preserved isotopic composition and
- 2 implications for paleoelevation estimates in central Tibet
- 3 Lin Li<sup>1,\*</sup>, Jay Quade<sup>1</sup>, Carmala Garzione<sup>1</sup>, William F. Defliese<sup>2</sup>, Peter DeCelles<sup>1</sup>, Paul Kapp<sup>1</sup>
- <sup>1</sup>Department of Geosciences, University of Arizona, Tucson, AZ 85721, USA
- 5 <sup>2</sup>School of the Environment, University of Queensland, Brisbane, QLD 4072, Australia
- 6 \*Corresponding author email: linli2@arizona.edu

7

8

9

10

11 12

13

14

15 16

17 18

19 20

21

22

23

24

25

2627

28

29

30

31

32

### Abstract

Paleoelevation and paleoclimate reconstructions based on carbonate proxies rely on the preservation of syndepositional surface water isotopic signatures. This study investigates the reliability of fine-grained carbonates (micrites) in recording well-preserved isotopic composition. Utilizing a suite of research tools, including petrography, X-ray diffraction mineralogy, stable isotopes, clumped isotope temperatures, isotope mixing, solid-state bond reordering modeling, and trace element concentrations, we examine the diagenetic history of late Oligocene micritic carbonates from the Nima Basin in central Tibet. Our findings reveal that the lacustrine carbonates at deposition were micritic and calcite-dominated. However, they underwent partial dolomitization through cryptic recrystallization during shallow burial at temperatures of ~34-40 °C, likely influenced by groundwaters with abundant Mg<sup>2+</sup> and trace elements distinct from surface waters. Subsequently, during the further burial at temperatures of ~120–130 °C, vein calcites precipitated from thermal fluids. Concurrently, the calcite component of fluid-adjacent micrites underwent open-system recrystallization, recording temperatures of 100-130 °C, while the associated dolomite component remained minimally altered due to its higher resistance to dissolution. In contrast, micritic calcites unaffected by thermal fluids experienced partial solid-state bond reordering that elevated clumped isotope temperatures to 50–60 °C. This study underscores the complex diagenetic histories that micrites can undergo, emphasizing the need for caution when interpreting carbonate stable oxygen isotopes in paleoclimate and paleoelevation studies, especially in tectonically active regions. Finally, our analysis infers that the stable oxygen isotopic values of the calcitic soil carbonates in the Nima Basin are well-preserved and reflect moderately high paleoelevations of ~3.3 km at 26–25 Ma. This suggests a >1 km elevation gain during the Neogene, highlighting subsurface geodynamic processes as additional drivers of surface uplift in central Tibet.

33

34

## **Keywords:**

35 Micrite, diagenesis, clumped isotopes, dolomitization, solid-state bond reordering, paleoelevation

### 1. Introduction

Quantitative stable isotope-based paleoaltimetry has received considerable attention during the last two decades, because of its significance to geodynamic history, to regional and global climate changes, and to biodiversity (An et al., 2001; Ding et al., 2022; Garzione et al., 2017; Raymo and Ruddiman, 1992; Spicer et al., 2020). For example, reconstructed surface uplift histories have been used to infer that both upper-crustal shortening and sub-surface geodynamic processes (crustal flow and sinking of lower lithosphere) contributed to the topographic growth of the South American Andes and Tibetan Plateau (Ding et al., 2022; Garzione et al., 2017; Li and Garzione, 2023). Surface uplift of the Tibetan Plateau has also been widely considered a major player in shaping the Cenozoic climate system of Asia, including the initiation and intensification of summer monsoon systems in South and East Asia as well as aridification of central Asia (An et al., 2001; Kutzbach et al., 1993; Molnar et al., 2010; Wu et al., 2022).

Among the many proxies used to reconstruct paleoelevations, such as organic lipids, fossils, and hydrothermal silicates, authigenic carbonates (e.g., lacustrine and paleosol carbonates) have been the most widely used, as both their stable oxygen isotopes ( $\delta^{18}O_{carb}$ ) and clumped isotope temperatures can be used for paleoelevation estimates (Huntington and Lechler, 2015; Rowley and Garzione, 2007). To derive reliable paleoelevations, carbonate rocks need to retain syndepositional Earth-surface isotope signatures, although it is widely known that carbonate minerals and rocks are prone to diagenesis (Armenteros, 2010; Garzione et al., 2004; Immenhauser, 2022; Longman, 1980; Quade et al., 2020; Swart, 2015; Tucker, 1990).

Depending on the timing and environment, diagenesis can occur in three broad stages (Armenteros, 2010; Choquette and Pray, 1970): 1) eogenesis occurs shortly after deposition when the carbonates are still shallowly buried and in the presence of surface waters; 2) mesogenesis indicates alteration during moderate to deep burial with elevated temperatures and with or without the presence of fluids that are probably different from surface waters; and 3) telogenesis is the alteration during or after exhumation to the Earth-surface. It is essential to identify whether carbonates experienced diagenesis after deposition, and the stages of diagenesis, as this will determine the evolution of stable and clumped isotopic values. For example, although mesogenesis usually indicates alteration of precursor isotope signatures, if it occurred in a closed system or the carbonates only experienced solid-state bond reordering, the stable isotopes wouldn't be changed, but still reflect syndepositional Earth-surface water signatures (Huntington and Lechler, 2015).

Numerous quantitative paleoelevation studies based on either the stable or clumped isotopes of carbonates have been conducted in the Tibetan Plateau (see reviews in Ding et al., 2022; Li et al., 2022). With few exceptions, most of the studies inferred well-preserved carbonate stable isotope signals based on the preservation of micritic textures using a petrographic microscope and/or cathodoluminescence imaging. However, the preservation of micritic textures alone is not sufficient to determine whether isotopic signals are well-preserved (Leier et al., 2009; Winkelstern and Lohmann, 2016). In recent years, the integrated analyses of stable and clumped isotopes have increased our ability to identify diagenetic alteration (Bergman et al., 2013; Dale et al., 2014; Ingalls et al., 2020; Lacroix and Niemi, 2019; Ryb et al., 2021; Shenton et al., 2015; Veillard et al., 2019; Winkelstern and Lohmann, 2016). Additionally, research tools such as carbonate U-Pb

dating (Cong et al., 2021; Hagen-Peter et al., 2021; Lawson et al., 2018; Mangenot et al., 2018) and electron microscope techniques (Ingalls and Snell, 2021; Li et al., 2019) provide new opportunities to identify different diagenetic stages, as well as to observe diagenetic features at much finer scales, i.e., micritic textures.

A major purpose of this study is to explore the reliability of fine-grained micritic carbonates (micrites) in recording well-preserved isotopic composition. We choose the Nima Basin in central Tibet (Fig. 1A) as a case study. Previously, DeCelles et al. (2007b) reported  $\delta^{18}O_{carb}$  values of pedogenic carbonates as low as -18% (VPDB) from the 4DC section (Fig. 1B), which was used to infer the attainment of similar-to-present high elevations of central Tibet since ~25 Ma. Later, Huntington et al. (2014) reported clumped isotope temperatures from lacustrine carbonates of the same 4DC section, which exhibited higher than Earth-surface temperatures of 40–60 °C and were interpreted to indicate closed-system cryptic recrystallization. This study aims to explore further the diagenetic history of the 4DC section for three reasons. First, in the 4DC section of the Nima Basin, vein calcites exist in many stratigraphic levels and exhibit very negative  $\delta^{18}O_{carb}$  values, i.e., -19‰ (DeCelles et al., 2007b). The potential influence of the vein calcite-associated diagenesis on surrounding micrites has not been explored. Second, recent studies in southern Tibet, especially along the Indus-Yarlung suture zone, emphasize extensive late-stage carbonate diagenesis due to deformation and magmatism, which casts doubt on previous paleoelevation reconstructions in that region (Huang et al., 2022; Ingalls, 2019; Leier et al., 2009; Quade et al., 2020). Third, the paleoelevation history of central Tibet is still widely debated despite considerable recent efforts (see reviews in Li et al., 2022), which hinders our understanding of the mechanisms of the Tibetan Plateau growth (Ding et al., 2022; Li et al., 2022).

In this study, we report additional clumped isotope temperatures from both lacustrine micrites and vein calcites, as well as one paleosol nodular carbonate, from the 4DC section, Nima Basin, using laser-based spectroscopy developed at the University of Arizona (Wang et al., 2020; Yanay et al., 2022). We aim to explore the diagenetic history of micritic carbonates and their implications for previous paleoelevation estimates. In combination with X-ray diffraction (XRD) mineralogy, petrographic observation, scanning electron microscope (SEM), electron probe microanalysis (EPMA), stable isotopes, isotope mixing, solid-state bond reordering modeling, and carbonate LA-ICP-MS trace element analyses, we illuminate a more complete and complex carbonate diagenetic history that includes at least two distinct burial diagenesis stages: shallow burial partial dolomitization and moderately burial open-system recrystallization and solid-state bond reordering. We further discuss potential variations of both stable isotopes and clumped isotopes during these different stages of diagenesis. Finally, with this new understanding, we reinterpret previous paleoelevation data and obtained a ~3.3 km paleoelevation at 26–25 Ma, which requires a >1 km elevation gain during the Neogene and subsurface geodynamic processes as additional drivers of surface uplift in central Tibet.

### 2. Geologic setting

The Nima Basin is located in central Tibet along the Bangong suture zone (Fig. 1A), which marks the Late Jurassic–Early Cretaceous westward, diachronous collision between the Lhasa and Qiangtang terranes (Kapp and DeCelles, 2019; Yin and Harrison, 2000). The modern basin is ~150

km long from east to west, and ~50 km wide from north to south. Restored balanced-cross sections indicate that the basin was originally >110 km wide during the mid-Cretaceous, in response to the flexural loading of the north-dipping Muggar thrust (a section of the Shiquanhe-Gerze-Amdo thrust system) on the north and the south-dipping Gerze-Seling Co backthrust on the south (Kapp et al., 2007; Kapp et al., 2005). The basin was partitioned into the northern and southern sub-basins by internal shortening since Late Cretaceous time (DeCelles et al., 2007a; Kapp et al., 2007). Contractional deformation and concomitant sedimentary deposition lasted until the Miocene. Paleocurrent and provenance studies indicate that the southern and northern Nima basins received detritus dominantly from the south and north of the basin, respectively (DeCelles et al., 2007a).

In the southern Nima Basin, Oligocene–Miocene strata of the Nima Redbed Unit vary along strikes (DeCelles et al., 2007a). Strata to the west and south of Nima town are dominated by sandstone and siltstone that are interpreted to represent fluvial sedimentary systems, with channel, overbank floodplain, and crevasse-splay deposits. East of Nima town, the 1DC and 4DC sections are dominated by fan-delta and fine-grained lacustrine deposits (DeCelles et al., 2007a). In the 4DC section, thin yellowish gray-colored lacustrine marl beds are interbedded with massive brick red-colored siltstones (Fig. 2A) and well-developed calcisols with pedogenic carbonate nodules (DeCelles et al., 2007b). This study focuses on the lacustrine marls (micritic carbonate) of the 4DC section. Secondary vein calcites are observed in many stratigraphic levels and can be abundant in certain layers (Fig. 2B).

No absolute age constraints are available for the 4DC section. However, tuffs from the adjacent 1DC section (Fig. 1B) that are at similar stratigraphic levels as the 4DC section yield biotite  $^{40}$ Ar/ $^{39}$ Ar ages of  $25.8 \pm 0.2$  Ma and  $24.9 \pm 0.1$  Ma (DeCelles et al., 2007b). The depositional ages of the 4DC section are thus inferred to be late Oligocene. Carbonate U-Pb analyses were conducted on three lacustrine micrite samples from the 4DC section, but they yielded ages with large uncertainties (see section 4.7 for details).

### 3. Methods

# 3.1 Petrographic, CL, SEM, and mineralogical analysis

Polished thin sections were made from five selected carbonate samples and were observed under a petrographic microscope using both plain- and cross-polarized light at the University of Arizona. A Reliotron cold cathodoluminoscope operated at an acceleration voltage of 7–9 kV and a beam current intensity of 0.3–0.5 mA was used to examine the luminescence of the same thin sections at the University of Texas at Arlington. Scanning electron microscopy (SEM) was conducted using an FEI Helios NanoLab 660, housed in the Kuiper Imaging Facility at the University of Arizona, under a voltage of 5 kV and a current of 0.2 nA.

Eight carbonate samples were powdered for XRD analysis to determine mineralogy. The experiments were conducted using a Philips PANalytical X'Pert PRO MPD instrument in the Department of Chemistry and Biochemistry at the University of Arizona. The X-ray radiation wavelength was about 1.54 Angstroms (Å) (copper Ka radiation generated by a sealed X-ray tube with copper anode), and the Bragg-Brentano theta-theta geometry was used in the measurements.

Semiquantitative estimates of the weight percentage (wt%) of each mineral present were estimated using the reference intensity ratio (RIR) available in the XRD database. The wt% is proportional to the (XRD intensity)/RIR. All wt% values were normalized in such a way that the sum of all entries equals 100%.

### 3.2 EPMA element mapping

Two carbonate samples were selected for element mapping using an Electron Probe Micro-Analyzer (EPMA). Rock slabs were polished, carbon coated, and then analyzed at the Kuiper Imaging Facility at the University of Arizona using a Cameca SX-100 Ultra instrument. For all element maps, the instrument was configured to 15 kilovolts (kV) and 40 nanoamperes (nA). The magnesium (Mg), calcium (Ca), manganese (Mn), strontium (Sr), and iron (Fe) elements were collected using wavelength-dispersive spectrometers; while the silicon (Si), chromium (Cr), barium (Ba), and sometimes molybdenum (Mo) elements were collected using energy-dispersive spectrometers. For the high-resolution element maps, 1024 pixels per line, 40 micron beam size, and 10 milliseconds (ms) dwell time were used; for the medium-resolution element maps, 512 pixels per line, 80 micron beam size, and 20 ms dwell time were used.

# 3.3 Carbonate clumped isotope analysis

Carbonate clumped isotope ( $^{13}\text{C-}^{18}\text{O}$  bonds,  $\Delta_{638}$ ) content in excess of the stochastic distribution was measured at the Environmental Isotope Laboratory at the University of Arizona, using a tunable infrared laser differential spectrometer (TILDAS) constructed by Aerodyne Research, Boston. The term  $\Delta_{638}$  is the laser measurement equivalent of  $\Delta_{47}$  in mass spectrometry-based analysis.

About 2 mg of powdered carbonate was reacted with dehydrated phosphoric acid under vacuum at 70 °C. The conventional isotope ratio measurement relative to VPDB was calibrated based on repeated measurements of International Atomic Energy Agency (IAEA) reference materials. Clumped isotope values ( $\Delta_{638}$ ) are reported in the carbon dioxide equilibrium scale (CDES) theoretical reference frame defined by water-equilibrated gases, heated gases, and ETH 1–4 carbonate standards (Bernasconi et al., 2021; Dennis et al., 2011), and are reported for acid digestion at 70 °C (CDES<sub>70</sub>). The precisions for these measurements are  $\pm 0.023\%$  for  $\Delta_{638}$ ,  $\pm 0.04\%$  for  $\delta^{18}$ O, and  $\pm 0.03\%$  for  $\delta^{13}$ C (pooled reproducibility, 1-sigma), respectively. The laser-based  $\Delta_{638}$  – temperature relationship for carbonates is based on fifty-one synthetic calcites that equilibrated at temperatures from 6 °C to 1100 °C (Yanay et al., 2022):

```
\Delta_{638\text{CDES}} = (0.0409 \pm 0.0003) \times (10^6/\text{T}^2) + (0.1776 \pm 0.0031), R^2 = 0.997 equation (1)
```

T in this equation is referred to throughout the text as  $T_{(\Delta638)}$ , thus distinguishing measurements made by the laser system versus mass spectrometry,  $T_{(\Delta47)}$  (Ghosh et al., 2006), although  $T_{(\Delta47)}$  and  $T_{(\Delta638)}$  have been shown to be statistically equivalent (Yanay et al., 2022). Equation (1) is within error of recent mass spectrometry-based  $\Delta_{47}$  – temperature relationships and

correctly predicted precipitation temperatures for a suite of seventeen natural carbonates for both calcite and aragonite (Yanay et al., 2022). Complete details of this method and the calibration of the temperature –  $\Delta_{638}$  relationship are described in Wang et al. (2020) and Yanay et al. (2022).

For two of the samples, 4DC34 and 4DC41B, which contain both calcite and dolomite components, we used 0.5 mol acetic acid to process the bulk micrite to preferentially remove the calcite component from the dolomite component. Excess (>2–3 ml) acetic acid was added to ~200 mg micrite powders and left at room temperature to react for either 60 minutes or 120 minutes. The remaining powders containing the dolomite component were cleaned with deionized water and dried for clumped isotope analysis. We acknowledge that this processing method may also dissolve a certain amount of dolomite, however, we consider the amount to be small as the reaction occurred at room temperatures with diluted acetic acid and a shorter duration.

All clumped isotope samples were analyzed for 5–7 replicates. Each replicate measurement was based on four comparisons (sub-cycles) of the sample and reference gas. We excluded replicates with fewer than two sub-cycles and outliers to calculate the mean value of each sample. The outlier was defined as follows: first, we calculated the average  $\Delta_{638}$  value of all replicates for each sample, then we calculated the difference of  $\Delta_{638}$  between each replicate with the average; and finally, we considered differences of >0.023 ( $\Delta_{638\text{CDES}}$  external standard deviation of references) as outliers, which corresponds to ~7 °C  $T_{(\Delta 638)}$  temperatures in the range of 0–100 °C. In total, seventy-six replicates were measured and ten replicates were excluded. All reported clumped isotope values were averaged from 4–5 replicates. Supplementary Data S1 lists all clumped isotope values, including excluded replicates, of all new samples; Supplementary Data S2 lists all clumped isotope data of standards (carbonate standards ETH1–4 and equilibrated gas) used for calibration.

### 3.4 Mixing model of stable and clumped isotopes

For samples containing both dolomite and calcite components, i.e., 4DC34 and 4DC41B, we measured the clumped isotopes for both the bulk sample and the dolomite component (section 3.3). We then calculated the  $\delta^{13}$ C,  $\delta^{18}$ O, and  $\Delta_{638}$  values of the calcite component using the mixing model of Defliese and Lohmann (2015). Leached dolomite samples that had been reacted with acetic acid to remove calcite were treated as end-member one, while the bulk carbonate was treated as the final mixture. The unknown calcite isotopic values constituted end-member two. Percent contributions of each mineral end-member were estimated from XRD analysis (section 3.1). A goal-seeking algorithm was used to find the correct end-member values for the calcite in each sample that resulted in the measured bulk sediment isotopic values, solving in order for  $\delta^{13}$ C,  $\delta^{18}$ O, and finally  $\Delta_{638}$ . All mixing model results are presented in Supplementary Table S1.

### 3.5 Clumped isotope bond reordering modeling

Potential carbonate clumped isotope bond reordering due to burial was evaluated for samples in the 4DC section of the Nima Basin by constructing several thermal (burial and exhumation) histories and then analyzing them using the Isotopylog package for python from Hemingway and Henkes (2021) and using the kinetic parameters for either calcite or dolomite of Hemingway and

Henkes (2021), here referred to as "HH21" model. The HH21 model was chosen because it contains reordering kinetic parameters for both calcite and dolomite minerals and is also the most 'general' bond reordering model. The  $\Delta_{638}$  – temperature equation of Yanay et al. (2022) (equation 1 in this paper) was used for the equilibrium  $\Delta_{47}$  – temperature relationship, replacing the default equation of Anderson et al. (2021) in Hemingway and Henkes (2021). This may result in a small amount of error due to the differences between  $\Delta_{638}$  and  $\Delta_{47}$ , however, as shown in Yanay et al. (2022), such differences are minimal. Test runs using these two different clumped isotope temperature calibration equations yielded nearly identical results, as the much larger source of error is the uncertainty in the kinetic parameters of bond reordering. For this study, we conducted the following three groups of modeling runs.

The first group of modeling runs was for calcite. As the exact exhumation history of the 4DC section is unknown, we ran the models assuming the following three different burial and exhumation histories: S1, gradual burial of the 4DC section to maximum depth with maximum temperatures (varied by run) between 25 and 11 Ma, staying at maximum burial depth and temperature between 11 and 10 Ma, and exhumation to Earth-surface between 10 and 0 Ma; S2, gradual burial to maximum depth between 25 and 20 Ma, staying at maximum burial depth and temperature between 20 and 10 Ma, and exhumation to Earth-surface between 10 and 0 Ma; S3, gradual burial to maximum depth and temperature between 25 and 20 Ma, staying at maximum burial depth and temperature between 20 and 5 Ma, and exhumation to Earth-surface between 5 and 0 Ma. For each of the burial and exhumation scenarios, we first considered a 130 °C maximum burial temperature, assuming that the clumped isotope temperatures of the vein calcites represent the maximum burial temperature. The purpose of this run is to figure out the final clumped isotope temperatures of calcite under a 130 °C maximum burial temperature. Then we assumed that the  $T_{(\Lambda638)}$  values of 50 °C and 60 °C of the two lacustrine micritic calcite samples, i.e., 4DC51 and 4DC64, were caused by solid-state bond reordering, and solved for the maximum burial temperatures needed. As we also do not know the syndepositional  $T_{(\Delta 638)}$  temperatures, we assumed two possibilities, 20 °C or 30 °C, based on our studies of lacustrine carbonates of similar ages in the adjacent Lunpola Basin (Fig. 1A; data under review in another journal). In total, there are 18 separate model runs in this group (C1–C18 in Supplementary Table S2).

The second group of modeling runs was for dolomite. We first conducted eighteen model runs with configurations that are the same as C1–C18 but for dolomite (D1–D18 in Supplementary Table S2). In addition, we also carried out four more runs under the burial and exhumation scenario S2. We set the maximum burial temperatures in these runs the same as those needed to reorder calcite to 50 °C or 60 °C, i.e., similar maximum burial temperatures as in model runs C8, C11, C14, and C17. The purpose of these model runs was to figure out how much bond reordering dolomite would experience under the maximum burial temperatures that can reorder 20 ° or 30 °C calcite to 50 °C or 60 °C (D19–D22 in Supplementary Table S2).

The third group of modeling runs was designed to compare the differences between different models for calcite reordering. We compared three models that differ in their mechanistic interpretations of the solid-state bond reordering: the transient defect/equilibrium defect model (Henkes et al., 2014; Passey and Henkes, 2012), here referred to as "Hea14" model; the paired exchange-diffusion model (Stolper and Eiler, 2015), here referred to as "SE15" model; and the disordered kinetic model ("HH21" model) (Hemingway and Henkes, 2021). We compared the HH21, Hea14, and SE15 model results using the Isotopylogy software of Hemingway and Henkes

283 (2021). To minimize the influence of thermal history, for these model runs, we assumed the same burial and exhumation scenario S2 and maximum burial temperatures of 130 °C (C19–C22 in

Supplementary Table S2).

### 3.6 Carbonate LA-ICPMS analysis

Carbonate U-Pb analyses of three micrite and two vein calcite samples were performed at the University of California, Santa Barbara using a Photon Machines Excite 193 laser ablation system coupled to a Nu Instruments Plasma3D MC-ICP-MS, following the analytical procedures of Kylander-Clark (2020). Samples were analyzed in polished, one-inch epoxy mounts, using an 85 µm spot run at 10 Hz for 15 s following a 20 s baseline. Unknown analyses were corrected for instrument drift and mass bias in a two-step procedure using a combination of analyses from NIST614 glass and calcite standard WC-1 (254 Ma; Roberts et al., 2017) that were measured periodically throughout the analytical session; NIST614 was first used to correct for instrument drift of all isotopic ratios and the mass and detector bias of the <sup>207</sup>Pb/<sup>206</sup>Pb ratio using Iolite v2.5 (Paton et al., 2011), and a correction for the mass and detector bias of the <sup>206</sup>Pb/<sup>238</sup>U ratio was corrected such that, using an initial <sup>207</sup>Pb/<sup>206</sup>Pb ratio of 0.85, WC-1 yields 254 Ma. Analyses of calcite standards ASH 15D (2.965 Ma; Nuriel et al., 2021), and Duff Brown Tank (64 Ma; Hill et al., 2016) analyzed throughout the analytical session yielded ages that overlap within uncertainties of their accepted values. All data are presented in Supplementary Data S3.

### 4. Results

# 4.1 Petrographic, CL, SEM, and mineralogical results

Several different types of carbonate textures were observed under petrographic microscopes (Fig. 2C–F). For most of the samples, the bulk carbonate samples are dominated by micrite (Fig. 2D and 2F), while calcite veins are abundant in some samples (Fig. 2C). A few other samples, e.g., 4DC64, are dominated by microspars (Fig. 2E). No significant luminescence difference was observed between the vein calcite and adjacent micrite (Supplementary Fig. S1). SEM images show micro-crystals in the micrite adjacent to the vein calcite in sample 4DC41B (Fig. 2G), while 4DC51 is composed largely of calcite nanoparticles (Fig. 2H). See Supplementary Fig. S2 for more SEM images.

XRD analysis indicates that the analyzed carbonate samples have carbonate contents between 73% and 91%, with one exception (45%) (Table 1). Most of the lacustrine micrites are dominated by dolomite (61% to 93% of the carbonate content, with a mean of 74%); whereas samples 4DC51 and 4DC64 are nearly pure calcite (Table 1 and Fig. 3A). In the following, wherever "micritic calcite" is indicated, it refers to samples 4DC51 and 4DC64 that are nearly pure calcite in composition; wherever "calcite component" and "dolomite component" are indicated, they refer to the different carbonate species in micritic carbonates that contain both calcite and dolomite components, such as samples 4DC34 and 4DC41B. The one paleosol carbonate consists of pure calcite. Although we do not have XRD results for the vein carbonate, EPMA element analysis (see below) indicates that the veins are pure calcite, henceforth referred to as vein calcite.

323

324

325

326

327

328

329

330

331

332

333

334

### 4.2 EPMA element maps

For sample 4DC41A (collected at the same location as 4DC41B, but from two different hand samples), the EPMA element maps show clear differences between micrite and vein calcite (Fig. 2I-J). For example, the vein calcites show a distinct red color on the Ca map (Fig. 2I) and a black color on the Mg map (Fig. 2J), indicating a pure calcite component. The boundary between vein calcite and micrite is sharp with differences in concentration of Ca and Mg (Fig. 2I–J). Within micrite, the distribution of different elements is rather homogeneous. Sample 4DC47.2 shows a relatively homogeneous color in the Ca map (Fig. 2K), but visible changes in the Mg map (Fig. 2L) that probably reflect an inter-lamination compositional difference. Supplementary Figs. S3-S5 shows maps of other minor elements of these two samples, including another larger-scale element maps of 4DC41A.

335

336

337 338

339

340

341 342

343

344

345

346 347

348

349 350

351

352

353

354 355

356

### 4.3 Carbonate stable isotope data

Carbonate  $\delta^{18}O_{carb}$  and  $\delta^{13}C_{carb}$  values were measured at the same time as the clumped isotopes (Table 2). We combine these new stable isotopic data with those published in DeCelles et al. (2007b) to discuss the stable isotopic signatures (Fig. 3B-F; note that only lacustrine carbonates were considered here).

For the  $\delta^{18}O_{carb}$  values (VPDB) of micrites (Fig. 3C), the following features are observed: 1) large variations between -9\% and -14\% within a single hand sample but different laminae, e.g., at the stratigraphic level of 130 m; 2) excluding the bottom sample (4DC34) and another two in the lower part (4DC51 and 4DC64, outlined by a gray circle), the lowest  $\delta^{18}O_{carb}$  values show an upward decrease in  $\delta^{18}O_{carb}$  values (from -11.7% to -13.4%); and 3) samples 4DC51 and 4DC64 have the lowest  $\delta^{18}O_{carb}$  values of ~-16.5‰. The  $\delta^{13}C_{carb}$  values (VPDB) of micrites show the following features (Fig. 3D): 1) variations as large as 2% exist within a single hand sample but different laminae; 2) the bottom two samples (4DC34 and 4DC41A/B) show lower  $\delta^{13}C_{carb}$  values between -2% and -5%; and 3) all the other samples show similar  $\delta^{13}C_{carb}$  values between -1% and +1%, including 4DC51 and 4DC64.

For vein calcites, both their  $\delta^{18}O_{carb}$  and  $\delta^{13}C_{carb}$  values are consistent throughout the stratigraphic levels (Fig. 3E–F). The  $\delta^{18}O_{carb}$  values of vein calcites are lower (-14% to -19%) than those of micrites (Fig. 3B) while their  $\delta^{13}C_{carb}$  values (-2‰ to 0‰) are similar to those of micrites but with a smaller range (Fig 3B). On the  $\delta^{18}O_{carb}$  versus  $\delta^{13}C_{carb}$  graph (Fig. 3B), micrite and vein calcite samples generally do not overlap, although two of the micrite values (4DC51 and 4DC64, circled in gray) fall within the vein calcite domain.

### 4.4 Carbonate clumped isotope data

Previously, Huntington et al. (2014) also reported clumped isotope temperatures ( $T_{(\Delta47)}$ ) of lacustrine carbonates from the same 4DC section. It is noted that although not exactly the same, for most bulk samples that are analyzed in both Huntington et al. (2014) (solid blue circles, Fig. 4) and this study (solid orange circles), the  $T_{(\Delta638)}$  and  $T_{(\Delta47)}$  temperatures agree with each other within uncertainty. Supplementary Fig. S6 exhibits the  $T_{(\Delta638)}$  temperatures of the new samples that include all replicates (i.e., no outliers were removed), which shows nearly the same temperatures and trends compared to the data reported in Fig. 4. This comparison indicates that our method of removing outliers did not result in a bias to the data.

The new measurements of this study include two distinct groups of  $T_{(\Delta638)}$  temperatures: the vein calcites have  $T_{(\Delta638)}$  temperatures between  $119.5\pm8.0\,^{\circ}\text{C}$  and  $125.6\pm8.6\,^{\circ}\text{C}$  (solid red circles, Fig. 4) while the bulk micrites have relatively lower, but still higher than plausible Earth-surface  $T_{(\Delta638)}$  temperatures, between  $40.8\pm4.3\,^{\circ}\text{C}$  and  $63.2\pm5.1\,^{\circ}\text{C}$  (solid orange circles, Fig. 4). For samples that were treated with acetic acid to remove the calcite component, we note the remaining dolomite component has lower  $T_{(\Delta638)}$  temperatures than the bulk sample, but is still higher than plausible Earth-surface temperatures between  $40.1\pm4.2\,^{\circ}\text{C}$  and  $43.8\pm4.4\,^{\circ}\text{C}$ , except one lower value of  $34.4\pm3.9\,^{\circ}\text{C}$  (open orange circles, Fig. 4). The two lacustrine micritic calcite samples, 4DC51 and 4DC64, yielded  $T_{(\Delta638)}$  temperatures of  $49.7\pm3.7\,^{\circ}\text{C}$  and  $58.5\pm4.0\,^{\circ}\text{C}$  (Fig. 4, solid orange circles denoted by green arrows), and the one paleosol calcitic carbonate yielded a  $T_{(\Delta638)}$  temperature of  $41.1\pm4.2\,^{\circ}\text{C}$  (solid orange diamond denoted by a green arrow, Fig. 4).

**4.5 Results of mixing model** 

Using the mixing model described in section 3.4, we calculated the  $\Delta_{638}$  values and  $T_{(\Delta638)}$  temperatures for the calcite component of samples 4DC34 and 4DC41B, based on the measured  $\Delta_{638}$  values of the bulk sample and the dolomite component. For sample 4DC34, the dolomite component of which accounts for 79% (Table 1), we calculated the  $T_{(\Delta638)}$  temperature of the calcite component to be 102.9  $\pm$  36.7 °C and 68.5  $\pm$  39.0 °C (Fig. 4; open green circles; Supplementary Table S1). The two calculated values correspond to the two measured dolomite  $T_{(\Delta638)}$  temperatures (Table 2). For sample 4DC41B, which contains 66% dolomite component (Table 1), we calculated four  $T_{(\Delta638)}$  temperatures for the calcite component, as we obtained two  $T_{(\Delta638)}$  temperatures of the bulk sample and dolomite component, respectively (Table 2). The four calculated  $T_{(\Delta638)}$  temperatures of the calcite component of 4DC41B range between 98.3  $\pm$  22.9 °C and 127.8  $\pm$  21.8 °C (Fig. 4, open green circles). The large errors are associated with error propagation during calculations and incorporate the errors in the  $\Delta_{638}$  measurements.

### 4.6 Results of clumped isotope solid-state bond reordering

For model runs under different burial and exhumation histories (S1, S2, and S3), we observed, as expected, that under the same maximum burial temperatures, the longer the duration

of maximum burial, the higher the final modeled  $\Delta_{638}$  temperature is; and to obtain the same final modeled  $T_{(\Delta 638)}$  temperatures, it requires lower maximum burial temperatures for scenarios with longer durations of maximum burial (Supplementary Table S2). The differences in temperatures produced by different burial and exhumation histories are small (2–10 °C) compared to the measured  $T_{(\Delta 638)}$  temperature range, which also does not influence the following discussion of diagenetic history. We choose the modeling results of burial and exhumation scenario S2 (i.e., 25–20 Ma gradual burial, 20–10 Ma maximum burial at a constant temperature, 10–0 Ma exhumation to Earth-surface) for the following description and discussion, which we deem to be the most reasonable burial and exhumation history for the 4DC section based on our understanding of regional tectonic history.

According to the disordered kinetic model ("HH21" model) (Hemingway and Henkes, 2021), it was found that under 130 °C maximum burial temperatures, calcite with 30 °C (20 °C) temperatures would be reordered to 40 °C (31 °C) (Fig. 5A–B). It requires 144 °C (153 °C) maximum burial temperatures to reorder 30 °C (20 °C) calcite to 50 °C, while 154 °C (160 °C) is required to reorder 30 °C (20 °C) calcite to 60 °C (Fig. 5A–B). For dolomite, the model runs indicate that under 130 °C, 144 °C, and 154 °C maximum burial temperatures, 30 °C dolomite would be reordered to 31 °C, 33 °C, and 37 °C, respectively (Fig. 5C). If the dolomite temperature is 20 °C, under maximum burial temperatures of 130 °C, 153 °C, and 160 °C, the corresponding reordered temperatures are 21 °C, 27 °C, and 30 °C, respectively (Fig. 5D).

We found different results using different kinetic models (Fig. 6). Under 130 °C maximum burial temperatures, 30 °C calcite would be reordered to 40 °C, 53 °C, and 64 °C, respectively, using HH21, Hea14, and SE15 models (Fig. 6A–C). The reordered temperatures are 31 °C, 42 °C, and 57 °C for 20 °C calcite.

### 4.7 Carbonate LA-ICPMS data

Carbonate LA-ICPMS analyses were conducted with two main purposes: first, to constrain the depositional ages of micrite and precipitation ages of vein calcite using the U-Pb dating system; and second, to use the trace element concentration to characterize the fluid in which micrite and vein calcite were deposited. Due to the abundance of common Pb, as well as the small range of  $^{238}$ U/ $^{206}$ Pb ratios, the calculated carbonate U-Pb ages yield large uncertainties (Supplementary Fig. S7). Nonetheless, two of the samples (4DC34 and 4DC41B) yielded dates of  $30.0 \pm 6.5$  Ma and  $39.2 \pm 13.3$  Ma, older than but within uncertainty of the inferred ~26 Ma depositional age of the studied strata (DeCelles et al., 2007b). The vein calcites yielded precipitation ages of  $12.9 \pm 11.9$  Ma. We emphasize that the imprecise ages of the 4DC section do not influence the diagenetic history that will be discussed later.

Trace elements U and Th show distinct differences between micrites and vein calcites (Fig. 7). All three micrite samples have high U content with means at  $7.8 \pm 1.1$  ppm,  $28.1 \pm 3.2$  ppm, and  $46.0 \pm 4.6$  ppm, respectively. Similarly, all three micrite samples also have high Th content with means at  $2.8 \pm 1.8$  ppm,  $31.5 \pm 7.3$  ppm, and  $30.9 \pm 6.8$  ppm, respectively (Fig. 7). In contrast, the vein calcites have much lower U and Th content, with means at  $2.5 \pm 1.8$  ppm and  $0.5 \pm 0.2$  ppm for U, and  $0.1 \pm 0.3$  ppm and  $0.2 \pm 0.3$  ppm for Th (Fig. 7).

### 5. Discussion

### 5.1 Diagenetic history

Nearly all the analyzed carbonates in the 4DC section, whether lacustrine or paleosol carbonate in origin, and whether dolomite or calcite in composition, show higher-than-plausible Earth-surface  $T_{(\Delta638)}$  temperatures of >40 °C (Fig. 4), which are signs of diagenesis. The much higher 120–130 °C  $T_{(\Delta638)}$  temperatures of the vein calcites also indicate the existence of high-temperature thermal fluid, which may have also exerted diagenetic influences on adjacent micritic carbonates. In the following, we aim to identify possible processes that caused the diagenesis of the 4DC section carbonates. More specifically, we try to explain the following observations: 1) the dolomite components have  $T_{(\Delta638)}$  temperatures of 34–43 °C; 2) the associated calcite components have  $T_{(\Delta638)}$  temperatures of ~100–130 °C; 3) the two lacustrine micritic calcite samples have  $T_{(\Delta638)}$  temperatures of ~50–60 °C while the one paleosol calcitic carbonate has  $T_{(\Delta638)}$  temperature of ~41 °C; and 4) the vein calcites have  $T_{(\Delta638)}$  temperatures of ~120–130 °C (Fig. 4 and Table 2).

# 5.1.1 Shallow burial diagenesis (partial dolomitization)

XRD analysis indicates that except for the paleosol carbonate (4DC16) and two lacustrine micrites (4DC51 and 4DC64) that are calcite in composition, most analyzed lacustrine micrites are composed predominantly of dolomite (61–93%), with a smaller amount of calcite component (Table 1). Although modern Earth-surface conditions make direct dolomite precipitation difficult, ample evidence of dolomite precipitation from surface waters in the geologic past has been documented (Vasconcelos et al., 1995; Warren, 2000). As a result, it is possible that both the calcite and dolomite components were primarily deposited from lake water; or alternatively, the calcite component was primarily deposited, while the dolomite component was formed by partial dolomitization of the calcite in a later stage (Machel, 2004; Warren, 2000).

The trace element concentration of the micrites indicates that the dolomite was probably not primarily precipitated from lake water. The three micrite samples have high to very high concentrations of U, i.e.,  $\sim 7.8 \pm 1.1$  ppm,  $28.1 \pm 3.2$ , and  $46.0 \pm 4.6$  ppm, respectively (Fig. 7). Similarly, the Th concentration is also high to very high between  $2.8 \pm 1.8$  ppm and  $31.5 \pm 7.3$  ppm (Fig. 7). Normally, carbonate precipitated from Earth-surface lake waters contain U and Th concentrations that are no more than 1 ppm (Elisha et al., 2021; Roberts et al., 2020) due to the fact that lake water contains very low amounts of U and Th, i.e., a few to tens of ppb (Smedley and Kinniburgh, 2023; Waseem et al., 2015). This suggests that the dolomite is most likely formed by partial dolomitization in fluid that is different from surface lake waters and is a significant source of trace elements and other elements, such as Mg. Numerous studies have shown that when the supply of Mg<sup>2+</sup> ions in surrounding fluids is sufficient, calcite minerals may experience dolomitization (Machel, 2004; Warren, 2000).

Among the four measured  $T_{(\Delta638)}$  temperatures of the dolomite component, three of them are between 40–43 °C, and the other one is ~34 °C (Fig. 4 and Table 2). This indicates that the

dolomitization process occurred during shallow burial with slightly elevated ambient temperatures. As will be discussed in the next section, we consider that the 4DC section was further buried to a depth with a maximum temperature of ~130 °C. Under this burial temperature, the dolomite component would experience minimal bond reordering, i.e., ~1 °C increase of  $T_{(\Delta638)}$  temperatures (Fig. 5C–D). Thus, we suggest that partial dolomitization occurred at shallow depths equivalent to ambient temperatures of ~34–40 °C and that the dolomite component was largely unaffected by subsequent diagenetic events.

Although shallow burial partial dolomitization is our preferred explanation, it is conceivable that the measured 34–40 °C  $T_{(\Delta638)}$  temperatures represent a mixture of depositional (~20–30 °C) and early diagenetic secondary dolomite (e.g., ~50 °C). The exact burial temperatures at which partial dolomitization occurred would then be determined by the mixing ratios of these two stages of dolomite, although there is no firm evidence at this time for two stages of dolomite precipitation.

## 5.1.2 Deep burial diagenesis (solid-state bond reordering and open-system recrystallization)

Using mixing models (section 4.5), it is shown that the calcite component of samples 4DC34 and 4DC41B have  $T_{(\Delta638)}$  temperatures mainly ranging between 100 and 130 °C (Fig. 4, open green circles; Supplementary Table S1). However, the measured  $T_{(\Delta638)}$  temperatures of two lacustrine micritic calcite samples (4DC51 and 4DC64) of the same section are only 50–60 °C (Fig. 4, solid orange circles denoted by green arrows; Table 2). What caused the diverging  $T_{(\Delta638)}$  temperatures of the micritic calcite versus calcite component?

Solid-state bond reordering modeling indicates that if the 4DC section was buried to temperatures of 144–160 °C, 20–30 °C calcite would be reordered to 50–60 °C, e.g., 4DC51 and 4DC64 (Fig. 5A–B). The dominance of nanoparticles of sample 4DC51 under SEM (i.e., 10s–100s nanometers in scale; Fig. 2H) indicates the lack of post-depositional recrystallization, supporting this inference of bond-reordering only. Solid-state bond reordering can explain the  $T_{(\Lambda638)}$ temperatures of 4DC51 and 4DC64, however, it cannot explain the 100–130 °C  $T_{(\Delta638)}$ temperatures of the calcite component of 4DC34 and 4DC41B. We note that 4DC34 and 4DC41B contain abundant vein calcites (Fig. 2C), which exhibit 120–130 °C T<sub>(Δ638)</sub> temperatures (Fig. 4, solid red circles), indicating the presence of high-temperature thermal fluid. Thus, a possible explanation is that the calcite component of these two samples experienced open-system recrystallization (dissolution and reprecipitation) in the presence of high-temperature thermal fluids. As a result, the recrystallized calcite component would record similar 120-130 °C temperatures as the thermal fluid. The lower  $T_{(\Lambda 638)}$  temperatures of the calcite component, i.e., ~100 °C and 68 °C (Supplementary Table S1), can be explained as a mixing of depositional calcite and recrystallized calcite. This explanation receives support from SEM observations, which show micro-crystals probably formed during recrystallization (Fig. 2G). Additional supporting evidence of open-system recrystallization is the positive  $\delta^{18}O_{mw}$  values (-0.4  $\pm$  2.6 ‰, VSMOW) of water calculated from the  $\delta^{18}O_{carb}$  and  $T_{(\Delta 638)}$  temperatures of the calcite component (Supplementary Table S1), which is similar to the fluid in which vein calcite precipitated (-1.7  $\pm$  0.5%, Table 2), but different from those in which the dolomite component precipitated (-8.8  $\pm$  2.2 ‰, Table 2).

Although the calcite component of these samples experienced open-system recrystallization, we argue that the dolomite component in the same micrite samples did not recrystallize, based on the observation that these dolomites exhibit  $34-40\,^{\circ}\text{C}$  T<sub>( $\Delta638$ )</sub> temperatures (Fig. 4, open orange circles). Compared to calcite, dolomite has a higher resistance to dissolution (Langmuir, 1997) and thus a higher potential to remain unaltered (i.e., Mueller et al., 2020). Open-system recrystallization did not influence the two micritic calcite samples that lack vein calcite (4DC51 and 4DC64; Fig. 2E), further implicating the influence of high-temperature fluids in altering samples that do contain vein calcite.

The above discussion of solid-state bond reordering is based on the HH21 model of Hemingway and Henkes (2021), which requires 140–160 °C maximum burial temperatures to reorder 20–30 °C calcite to 50–60 °C (Fig. 5A–B). However, if using different models, such as Hea14 (Henkes et al., 2014) and SE15 (Stolper and Eiler, 2015), the results are slightly different. For example, under a 130 °C maximum burial temperature, the Hea14 model predicts that 30 °C calcite could be reordered to 53 °C (Fig. 6B); while the SE15 model predicts that 20 ° and 30 °C calcite could be reordered to 57 °C and 64 °C, respectively (Fig. 6C). The differences between these different models lie in their different mechanistic interpretations of solid-state bond reordering in calcite. If the kinetic parameters of the micritic calcite of 4DC51 and 4DC64 are more similar to those of Hea14 and SE15 models, it would indicate that the 4DC section does not need to be buried to the depth with 144–160 °C temperatures (as inferred from the HH21 model, Fig. 5A–B), but rather a temperature of 130 °C would be sufficient to reorder 20–30 °C micritic calcite to 50–60 °C (Fig. 6B–C).

Although both 144–160 °C and 130 °C maximum burial temperatures are possible to explain the 50–60 °C  $T_{(\Delta638)}$  temperatures of 4DC51 and 4DC64, we prefer the 130 °C scenario, as it is a simpler explanation for all the following three observations: 1) reorder micritic calcite samples 4DC51 and 4DC64 to 50–60 °C by solid-state bond reordering; 2) form the 120–130 °C vein calcite; and 3) reset the temperatures of the calcite component of samples 4DC34 and 4DC41B to 100–130 °C through open-system recrystallization. Considering the total measurable overburden of ~3 km or less based on the maximum thickness of younger strata in the Nima area (DeCelles et al., 2007a; Huntington et al., 2014), as well as possible thrust loading of the north-verging GSBT (Fig. 1A) (DeCelles et al., 2007a; DeCelles et al., 2007b; Kapp et al., 2007), it is reasonable that the 4DC section was buried to ~3.3–4.4 km depth with maximum burial temperatures of 120–130 °C, assuming a surface temperature of 20–30 °C, and a thermal gradient of 25–30 °C/km.

# 5.1.3 Summary of a multi-stage diagenetic history

Based on the above discussion, we summarize the most likely diagenetic history for the Nima Basin 4DC section carbonates (Fig. 8), as well as changes in both the  $\delta^{18}O_{carb}$  and  $T_{(\Delta638)}$  temperatures (Table 3).

During the late Oligocene (~26–25 Ma), limestones were deposited in the Nima Lake (T0 in Table 3 and Fig. 8) at Earth-surface conditions, such that both the stable and clumped isotopes of the limestone (micritic calcite) recorded the isotopic composition and temperature of lake water. Later, when the lacustrine limestone was shallowly buried to a depth with temperatures of 34–

40 °C, basinal fluid with  $Mg^{2+}$  ions and with different chemical compositions from surface lake waters, filled pore spaces and caused partial dolomitization of the micritic calcite (T1 in Table 3 and Fig. 8). Some layers experienced no dolomitization, such as 4DC51 and 4DC64. The newly formed dolomite component recorded the stable and clumped isotopes of the basinal fluid and shallow burial temperatures, respectively, whereas the remaining calcite experienced no changes and its stable and clumped isotopes still recorded surface lake water conditions. Considering the shallow burial depth of dolomitization, i.e., 0.3-0.8 km depth (considering surface temperatures of 20-30 °C, and thermal gradients of 25-30 °C/km), it is likely that the  $\delta^{18}O_{mw}$  values of the groundwater are similar as those of surface water, although there are additional inputs of trace elements.

With further burial, probably due to thrust loading from the south (DeCelles et al., 2007a; Kapp et al., 2007), the 4DC section was buried to a depth with temperatures of ~120–130 °C (T2, Table 3 and Fig. 8). Under these burial temperatures, the following diagenetic processes occurred: 1) the formation of 120–130 °C vein calcites, the stable and clumped isotope temperatures of which record those of the thermal fluid; 2) the micritic calcite samples that are far away from and unaffected by thermal fluid, e.g., 4DC51 and 4DC64, were reset to 50–60 °C temperatures by solid-state bond reordering; while their  $\delta^{18}O_{carb}$  and  $\delta^{13}C_{carb}$  values remain the same as depositional calcite; 3) the calcite components of micrites that are adjacent to and influenced by thermal fluid, e.g., 4DC34 and 4DC41B, were reset to 100–130 °C temperatures by open-system recrystallization; and 4) the associated dolomite components in these samples experienced neither open-system recrystallization nor solid-state bond reordering (i.e., only 1 °C temperature increase; Fig. 5C–D), due to the higher resistance to dissolution and bond reordering.

### 5.2 Implications for paleoelevation estimates of the Nima Basin in central Tibet

DeCelles et al. (2007b) interpreted the micritic texture of the paleosol carbonate (Supplementary Fig. S1A–B) of the 4DC section, in addition to a "conglomerate test", to reflect the preservation of syndepositional isotopic signals. They found very low  $\delta^{18}O_{carb}$  values, which are indistinguishable from the least evaporated  $\delta^{18}O_{carb}$  values of modern soil carbonates in the area. As a result, they deduced that the Nima Basin had reached its modern high elevations by at least 26 Ma. Subsequently, Huntington et al. (2014) determined >47 °C clumped isotope temperatures for the 4DC section lacustrine micrites. They concluded that varying degrees of micro-scale mineral recrystallization occurred in a rock-buffered environment and argued against the possibility of solid-state bond reordering.

This study reveals a more complex diagenetic history for the 4DC section carbonate rocks (Fig. 8). Compared to Huntington et al. (2014)'s study, the additional diagenetic processes were identified through: 1) a new XRD mineralogy study to identify both calcite and dolomite components, which is critical for both solid-state bond reordering modeling and differentiating phases of diagenesis; 2) updated model configuration and kinetic parameters for bond reordering, including the different reordering behaviors between calcite and dolomite (Hemingway and Henkes, 2021, and references within); and 3) additional clumped isotope measurements of the vein calcites. We do not favor a rock-buffered cryptic recrystallization explanation, because the process

of dolomitization, as well as the introduction of vein calcites, would require considerable fluid in the system, during both shallow and moderately deep burial.

Although at least two stages of diagenesis were identified for the Nima Basin 4DC section lacustrine carbonates, this does not necessarily negate DeCelles et al. (2007b)'s results, which used the very low  $\delta^{18}O_{carb}$  values of paleosol carbonate to infer similar-to-present high paleoelevations. As argued in section 5.1.3, in the 4DC section, the few pure calcite samples, e.g., 4DC16, 4DC51, and 4DC64 (Table 1), only experienced solid-state bond reordering, which would only influence the clumped isotope temperatures, but would not change the syndepositional  $\delta^{18}O_{carb}$  values. Thus, the argument for well-preserved  $\delta^{18}O_{carb}$  values in DeCelles et al. (2007b) would still hold. This inference confirms the reliability of the "conglomerate test" as originally proposed in DeCelles et al. (2007b) in detecting diagenesis, i.e., similar  $\delta^{18}O_{carb}$  values between newly deposited carbonates and interbedded marine limestone clasts strongly suggest diagenetic alteration.

As pointed out by Li et al. (2022), although the  $\delta^{18}O_{carb}$  values of soil carbonates are similar between 25–26 Ma and the present, this does not require that the region arrived at exactly the present elevation, as the temperature of soil carbonate formation is probably different between 25–26 Ma and the present. If using the 33.4  $\pm$  3.0 °C (n=3, 1 $\sigma$ ) clumped isotope temperatures of the upper Niubao paleosol carbonate in the adjacent Lunpola Basin (Ingalls et al., 2020), which has similar depositional ages of 26–23 Ma (Fang et al., 2020), this would suggest elevations of only 3.3  $\pm$  0.5 km following the calculation method outlined in Li et al. (2022). This indicates an additional >1 km elevation increase in the Nima Basin (~4.6 km modern elevation) after ~25 Ma.

This new moderate paleoelevation inference (3.3 ± 0.5 km at 25–26 Ma for the Nima Basin) agrees with recent paleoelevation estimates in the nearby Lunpola Basin (Fig. 1A) (Li et al., 2022; Sun et al., 2022). Together, these studies suggested: 1) the existence of a moderately high central valley not only in the Lunpola Basin, but also in the nearby Nima Basin, which probably extended farther west along the Bangong suture zone (Li et al., 2022); and 2) the central valley was uplifted to its current high elevations (4.5–4.7 km) during the Neogene, but not during the Oligocene (Xiong et al., 2022), or even the late Eocene (Ingalls et al., 2020; Rowley and Currie, 2006). As there is no evidence for major upper-crustal shortening in central Tibet since ~23 Ma (Kapp et al., 2007), Neogene surface uplift may be attributed to northward underthrusting of the Indian lower crust and/or middle-lower crustal flow from surrounding high-elevation mountain ranges, e.g., Gangdese and Tanggula (Fig. 1A) (Li et al., 2022). In addition, considering the thin lithosphere beneath central Tibet (McNamara et al., 1997), the convective removal of the lower lithosphere might have also contributed to the Neogene surface uplift.

# 5.3 Implications for carbonate diagenesis studies

The results of this study and many other studies (e.g., Ingalls, 2019; Lacroix and Niemi, 2019; Leier et al., 2009; Winkelstern and Lohmann, 2016) indicate that micritic carbonates may have experienced complex diagenetic alterations. However, the recording of higher than plausible Earth-surface clumped isotope temperatures is also not confirming evidence of the loss of syndepositional stable isotopic signals. The retention of micritic textures with higher clumped isotope temperatures could be formed by several different processes that have different influences

on the syndepositional stable isotopic values: 1) closed-system cryptic-recrystallization, 2) open-system cryptic-recrystallization, and 3) solid-state bond reordering. Closed-system recrystallization and solid-state bond reordering would only alter the clumped isotope values but exert no influence on the syndepositional stable isotopic signals, which is not the case for open-system recrystallization.

Petrographic and CL observations are useful tools in identifying the existence of external fluid (a sign of open-system diagenesis), which usually leaves vein calcite as a product. However, it is also possible that the fluid exerts no influence on host carbonate rocks if the fluid activity is transient or the host materials are resistant to dissolution, i.e., dolomite. The measurement of clumped isotope temperatures and U-Pb dating (MacDonald et al., 2019; Mangenot et al., 2018; Mueller et al., 2020; Pagel et al., 2018) on both host and vein carbonate, could provide additional constraints to evaluate the diagenesis history. It is suggested that in studies of carbonate diagenesis, when vein calcite is present, the measurement of both the temperature and timing of vein calcite formation is beneficial. Fluid inclusions may also be abundant in micrites and vein calcites. Analyses of the stable isotopes, trace elements, and temperatures of the fluids (Pettke et al., 2012) provide direct information about ancient fluid in which carbonate precipitated and thus could also help explore diagenetic history (e.g., Mueller et al., 2020; Mueller et al., 2022).

Clumped isotope solid-state bond reordering modeling (Hemingway and Henkes, 2021; Henkes et al., 2014; Stolper and Eiler, 2015) provides an additional powerful tool to examine the causes of diagenesis. There has been some recent data indicating that water and/or the exchangeable fraction of water can increase reordering rates (Brenner et al., 2018; Looser et al., 2023; Nooitgedacht et al., 2021; Perez-Beltran et al., 2023; Sun et al., 2023). However, the currently available bond reordering models are all based on the heating experiments of optical calcite and biogenic calcite, i.e., branchiopod and belemnite (Hemingway and Henkes, 2021; Henkes et al., 2014; Looser et al., 2023; Stolper and Eiler, 2015). Lacustrine micrites and soil carbonates may have increased surface area and/or biological matter that can help speed up bond reordering, but how that compares to optical calcites and organic-matrix biogenic calcites is unclear at this time. It is necessary to conduct more heating experiments on natural lacustrine micrite and soil carbonate samples. The one paleosol calcite sample (4DC16) has a  $T_{(\Delta638)}$  temperature of 41 °C, which is more than 10 °C lower than those of lacustrine micritic calcite samples (4DC51 and 4DC64) at 50–60 °C, further exemplifies the likely difference in kinetic parameters between different types of calcites that were formed in varying environments.

### 6. Conclusions

In this study, we applied an integrated suite of tools to explore micrite diagenesis, including: mineralogy identification (XRD analysis), petrographic, CL, SEM, and EPMA imaging, LA-ICPMS trace element analysis and U-Pb dating, stable isotopes, clumped isotopes, as well as mixing models and solid-state bond reordering modeling. Our results demonstrate two stages of diagenesis for the Nima Basin 4DC section carbonates: shallow burial (34–40 °C) partial dolomitization, and moderately deep burial (120–130 °C) bond reordering and open-system recrystallization.

For the Nima Basin, our new results indicate that the  $\delta^{18}O_{carb}$  values of paleosol carbonates (DeCelles et al., 2007b) recorded the syndepositional Earth-surface water stable isotope signals. However, the Nima Basin was probably only ~3.3 km high during the late Oligocene, requiring an additional >1 km of surface uplift during the Neogene. This is consistent with recent paleoelevation studies in the nearby Lunpola Basin, which requires subsurface geodynamic processes other than shortening for the Neogene surface uplift along the Bangong suture zone in central Tibet (Li et al., 2022).

### Acknowledgements

We thank Zhennan Wang and David Dettman for assistance with clumped isotope analysis, Nitzan Yanzan for discussion on solid-state bond reordering modeling, Majie Fan and Rijumon Nandy for assistance with CL imaging, Andrei Astashkin for XRD data collection, Kenneth Domanik for assistance with EPMA analysis, Zoe Zeszut for help with SEM imaging, and Andrew Kylander-Clark for assistance with carbonate LA-ICPMS analysis. We thank associate editor Adrian Immenhauser, Mathias Mueller and Ian Winkelstern for comments and suggestions that helped clarify the content of this study. This study is supported by NSF grants PIRE-1545859 and EAR-2048656.

# Data Availability

All data associated with this paper (Data S1: clumped isotope data of new samples; Data S2: clumped isotope data of standards; Data S3: carbonate LA-ICPMS U-Pb data) are available through Zenodo at: https://doi.org/10.5281/zenodo.10523691.

## Appendix A. Supplementary material

The supplementary file includes two tables and five figures: Table S1: Calculation of stable and clumped isotopes of calcite component using mixing model. Table S2: Summary of solid-state bond reordering modeling results. Fig. S1 shows the CL images of samples 4DC16 and 4DC41A. Fig. S2 shows the SEM images of samples 4DC41B and 4DC51. EPMA maps of all measured elements (Ca, Mg, Si, Fe, Mn, Sr, Cr, and Ba) for sample 4DC41A\_coarse scale (Fig. S2), 4DC41A\_fine scale (Fig. S3), 4DC47.2\_coarse scale (Fig. S4). Fig. S5 shows the comparison of clumped isotope values using different data processing methods. Fig. S6 shows the Tera-Wasserburg plots of carbonate U-Pb data. The supplementary file can be found online at xxx.

### 716 References

- An, Z.S., Kutzbach, J.E., Prell, W.L., Porter, S.C., 2001. Evolution of Asian monsoons and phased uplift of the Himalaya–Tibetan plateau since late Miocene times. Nature 411(6833), 62-66.
- Anderson, N.T., Kelson, J.R., Kele, S., Daëron, M., Bonifacie, M., Horita, J., Mackey, T.J., John,
- 720 C.M., Kluge, T., Petschnig, P., Jost, A.B., Huntington, K.W., Bernasconi, S.M., Bergmann,
- 721 K.D., 2021. A unified clumped isotope thermometer calibration (0.5–1,100°C) using
- carbonate-based standardization. Geophys. Res. Lett. 48(7), e2020GL092069.
- Armenteros, I., 2010. Diagenesis of carbonates in continental settings, in: Alonso-Zarza, A.M., Tanner, L.H. (Eds.), Carbonates in continental settings. Elsevier, pp. 61-151.
- Bergman, S.C., Huntington, K.W., Crider, J.G., 2013. Tracing paleofluid sources using clumped isotope thermometry of diagenetic cements along the Moab Fault, Utah. Am. J. Sci. 313(5),

727 490-515.

- 728 Bernasconi, S.M., Daëron, M., Bergmann, K.D., Bonifacie, M., Meckler, A.N., Affek, H.P.,
- Anderson, N., Bajnai, D., Barkan, E., Beverly, E., Blamart, D., Burgener, L., Calmels, D.,
- Chaduteau, C., Clog, M., Davidheiser-Kroll, B., Davies, A., Dux, F., Eiler, J., Elliott, B.,
- Fetrow, A.C., Fiebig, J., Goldberg, S., Hermoso, M., Huntington, K.W., Hyland, E., Ingalls,
- 732 M., Jaggi, M., John, C.M., Jost, A.B., Katz, S., Kelson, J.R., Kluge, T., Kocken, I.J., Laskar,
- A.H., Leutert, T.J., Liang, D., Lucarelli, J., Mackey, T.J., Mangenot, X., Meinicke, N.,
- Modestou, S., Muller, I.A., Murray, S., Neary, A., Packard, N., Passey, B.H., Pelletier, E.,
- Petersen, S., Piasecki, A., Schauer, A., Snell, K.E., Swart, P.K., Tripati, A., Upadhyay, D.,
- Vennemann, T., Winkelstern, I., Yarian, D., Yoshida, N., Zhang, N., Ziegler, M., 2021.
- 737 Intercarb: A community effort to improve interlaboratory standardization of the carbonate
- 738 clumped isotope thermometer using carbonate standards. Geochem. Geophys. Geosyst.
- 739 22(5), e2020GC009588.
- Brenner, D.C., Passey, B.H., Stolper, D.A., 2018. Influence of water on clumped-isotope bond reordering kinetics in calcite. Geochim. Cosmochim. Acta 224, 42-63.
- Choquette, P.W., Pray, L.C., 1970. Geologic nomenclature and classification of porosity in sedimentary carbonates. AAPG Bull. 54(2), 207-250.
- Cong, F., Tian, J., Hao, F., Licht, A., Liu, Y., Cao, Z., Eiler, J.M., 2021. A thermal pulse induced
- by a Permian mantle plume in the Tarim Basin, northwest China: Constraints from clumped
- isotope thermometry and in situ calcite U-Pb dating. J. Geophys. Res. Solid Earth 126(4),
- 747 e2020JB020636.
- Daëron, M., 2021. Full propagation of analytical uncertainties in Δ<sub>47</sub> measurements. Geochem.
   Geophys. Geosyst. 22(5), e2020GC009592.
- Dale, A., John, C.M., Mozley, P.S., Smalley, P.C., Muggeridge, A.H., 2014. Time-capsule
- 751 concretions: Unlocking burial diagenetic processes in the Mancos Shale using carbonate
- 752 clumped isotopes. Earth Planet. Sci. Lett. 394, 30-37.

- DeCelles, P.G., Kapp, P., Ding, L., Gehrels, G., 2007a. Late Cretaceous to middle Tertiary basin
- evolution in the central Tibetan Plateau: Changing environments in response to tectonic
- partitioning, aridification, and regional elevation gain. Geol. Soc. Am. Bull. 119(5-6), 654-
- 756 680.
- DeCelles, P.G., Quade, J., Kapp, P., Fan, M., Dettman, D.L., Ding, L., 2007b. High and dry in central Tibet during the Late Oligocene. Earth Planet. Sci. Lett. 253(3-4), 389-401.
- Defliese, W.F., Lohmann, K.C., 2015. Non-linear mixing effects on mass-47 CO<sub>2</sub> clumped isotope thermometry: Patterns and implications. Rapid Commun. Mass Spectrom. 29(9), 901-909.
- 761 Dennis, K.J., Affek, H.P., Passey, B.H., Schrag, D.P., Eiler, J.M., 2011. Defining an absolute
- reference frame for 'clumped' isotope studies of CO<sub>2</sub>. Geochim. Cosmochim. Acta 75(22),
- 763 7117-7131.
- Ding, L., Kapp, P., Cai, F., Garzione, C.N., Xiong, Z., Wang, H., Wang, C., 2022. Timing and mechanisms of Tibetan Plateau uplift. Nat. Rev. Earth Environ. 3, 652-667.
- Elisha, B., Nuriel, P., Kylander-Clark, A., Weinberger, R., 2021. Towards in situ U–Pb dating of dolomite. Geochronology 3(1), 337-349.
- Fang, X.M., Dupont-Nivet, G., Wang, C.S., Song, C.H., Meng, Q.Q., Zhang, W.L., Nie, J.S.,
- Zhang, T., Mao, Z.Q., Chen, Y., 2020. Revised chronology of central Tibet uplift (Lunpola
- 770 Basin). Sci. Adv. 6, eaba7298.
- Garzione, C.N., Dettman, D.L., Horton, B.K., 2004. Carbonate oxygen isotope paleoaltimetry:
- Evaluating the effect of diagenesis on paleoelevation estimates for the Tibetan Plateau.
- Palaeogeogr. Palaeoclimatol. Palaeoecol. 212(1-2), 119-140.
- Garzione, C.N., McQuarrie, N., Perez, N.D., Ehlers, T.A., Beck, S.L., Kar, N., Eichelberger, N.,
- Chapman, A.D., Ward, K.M., Ducea, M.N., Lease, R.O., Poulsen, C.J., Wagner, L.S., Saylor,
- J.E., Zandt, G., Horton, B.K., 2017. The tectonic evolution of the central Andean plateau
- and geodynamic implications for the growth of plateaus. Annu. Rev. Earth Planet. Sci. 45,
- 778 529-559.
- Ghosh, P., Adkins, J., Affek, H., Balta, B., Guo, W., Schauble, E.A., Schrag, D., Eiler, J.M., 2006.
- 780 13C-18O bonds in carbonate minerals: A new kind of paleothermometer. Geochim.
- 781 Cosmochim. Acta 70(6), 1439-1456.
- Hagen-Peter, G., Wang, Y., Hints, O., Prave, A.R., Lepland, A., 2021. Late diagenetic evolution
- of Ordovician limestones in the Baltoscandian Basin revealed through trace-element
- mapping and in situ U–Pb dating of calcite. Chem. Geol. 585, 120563.
- Hemingway, J.D., Henkes, G.A., 2021. A disordered kinetic model for clumped isotope bond
- reordering in carbonates. Earth Planet. Sci. Lett. 566, 116962.

- Henkes, G.A., Passey, B.H., Grossman, E.L., Shenton, B.J., Pérez-Huerta, A., Yancey, T.E., 2014.
- Temperature limits for preservation of primary calcite clumped isotope paleotemperatures.
- 789 Geochim. Cosmochim. Acta 139(5), 362-382.
- Hill, C.A., Polyak, V.J., Asmerom, Y., Provencio, P., 2016. Constraints on a late Cretaceous uplift,
- denudation, and incision of the Grand Canyon region, southwestern Colorado Plateau, USA,
- from U-Pb dating of lacustrine limestone. Tectonics 35(4), 896-906.
- Huang, W., Lippert, P.C., Reiners, P.W., Quade, J., Kapp, P., Ganerød, M., Guo, Z., van
- Hinsbergen, D.J.J., 2022. Hydrothermal events in the Linzizong Group: Implications for
- Paleogene exhumation and paleoaltimetry of the southern Tibetan Plateau. Earth Planet. Sci.
- 796 Lett. 583, 117390.
- Huntington, K.W., Lechler, A.R., 2015. Carbonate clumped isotope thermometry in continental tectonics. Tectonophysics 647–648, 1-20.
- 799 Huntington, K.W., Saylor, J., Quade, J., Hudson, A.M., 2014. High late Miocene-Pliocene
- 800 elevation of the Zhada Basin, southwestern Tibetan Plateau, from carbonate clumped isotope
- 801 thermometry. Geol. Soc. Am. Bull. 127(1-2), 181-199.
- 802 Immenhauser, A., 2022. On the delimitation of the carbonate burial realm. Depos. Rec. 8(2), 524-
- 803 574.
- 804 Ingalls, M., 2019. Reconstructing carbonate alteration histories in orogenic sedimentary basins:
- Xigaze forearc, southern Tibet. Geochim. Cosmochim. Acta 251, 284-300.
- 806 Ingalls, M., Rowley, D.B., Currie, B.S., Colman, A.S., 2020. Reconsidering the uplift history and
- peneplanation of the northern Lhasa terrane, Tibet. Am. J. Sci. 320(6), 479-532.
- 808 Ingalls, M., Snell, K.E., 2021. Tools for comprehensive assessment of fluid-mediated and solid-
- state alteration of carbonates used to reconstruct ancient elevation and environments. Front.
- 810 Earth Sci. 9, 623982.
- 811 Kapp, P., DeCelles, P.G., 2019. Mesozoic-Cenozoic geological evolution of the Himalayan-
- Tibetan orogen and working tectonic hypotheses. Am. J. Sci. 319(3), 159-254.
- Kapp, P., DeCelles, P.G., Gehrels, G.E., Heizler, M., Ding, L., 2007. Geological records of the
- Lhasa-Qiangtang and Indo-Asian collisions in the Nima area of central Tibet. Geol. Soc.
- 815 Am. Bull. 119(7-8), 917-933.
- 816 Kapp, P., Yin, A., Harrison, T.M., Ding, L., 2005. Cretaceous-Tertiary shortening, basin
- development, and volcanism in central Tibet. Geol. Soc. Am. Bull. 117(7-8), 865-878.
- Kutzbach, J., Prell, W., Ruddiman, W.F., 1993. Sensitivity of Eurasian climate to surface uplift of
- the Tibetan Plateau. J. Geol., 177-190.
- 820 Kylander-Clark, A.R.C., 2020. Expanding the limits of laser-ablation U–Pb calcite geochronology.
- 821 Geochronology 2(2), 343-354.

- Lacroix, B., Niemi, N.A., 2019. Investigating the effect of burial histories on the clumped isotope
- thermometer: An example from the Green River and Washakie Basins, Wyoming. Geochim.
- 824 Cosmochim. Acta 247, 40-58.
- 825 Langmuir, D., 1997. Aqueous Environmental Geochemistry. Prentice Hall: Upper Saddle River,
- New Jersey.
- Lawson, M., Shenton, B.J., Stolper, D.A., Eiler, J.M., Rasbury, E.T., Becker, T.P., Phillips-Lander,
- 828 C.M., Buono, A.S., Becker, S.P., Pottorf, R., Gray, G.G., Yurewicz, D., Gournay, J., 2018.
- Deciphering the diagenetic history of the El Abra Formation of eastern Mexico using
- reordered clumped isotope temperatures and U-Pb dating. GSA Bull. 130(3-4), 617-629.
- Leier, A., Quade, J., DeCelles, P., Kapp, P., 2009. Stable isotopic results from paleosol carbonate
- in South Asia: Paleoenvironmental reconstructions and selective alteration. Earth Planet. Sci.
- 833 Lett. 279(3), 242-254.
- Li, L., Garzione, C.N., 2023. Upward and outward growth of north-central Tibet: Mechanisms that
- build high elevation, low relief plateaus. Sci. Adv. 9, 3058.
- Li, L., Lu, H., Garzione, C.N., Fan, M.J., 2022. Cenozoic paleoelevation history of the Lunpola
- Basin in central Tibet: New evidence from volcanic glass hydrogen isotopes and a critical
- 838 review. Earth-Sci. Rev. 231, 104068.
- Li, S., Currie, B.S., Rowley, D.B., Ingalls, M., Qiu, L., Wu, Z., 2019. Diagenesis of shallowly
- buried Miocene lacustrine carbonates from the Hoh Xil Basin, northern Tibetan Plateau:
- Implications for stable-isotope-based elevation estimates. Sediment. Geol. 388, 20-36.
- Longman, M.W., 1980. Carbonate diagenetic textures from near-surface diagenetic environments.
- 843 AAPG Bull. 64(4), 461-487.
- Looser, N., Petschnig, P., Hemingway, J.D., Fernandez, A., Grafulha, L.M., Perez-Huerta, A.,
- Vickers, M.L., Price, G.D., Schmidt, M.W., Bernasconi, S.M., 2023. Thermally-induced
- section clumped isotope resetting in belemnite and optical calcites: Towards material-specific
- kinetics. Geochim. Cosmochim. Acta 350, 1-15.
- MacDonald, J.M., Faithfull, J.W., Roberts, N.M.W., Davies, A.J., Holdsworth, C.M., Newton, M.,
- Williamson, S., Boyce, A., John, C.M., 2019. Clumped-isotope palaeothermometry and LA-
- 850 ICP-MS U–Pb dating of lava-pile hydrothermal calcite veins. Contrib. Mineral. Petrol.
- 851 174(7), 1-15.
- Machel, H.G., 2004. Concepts and models of dolomitization: A critical reappraisal. Geol. Soc.,
- 853 London, Spec. Publ. 235(1), 7-63.
- Mangenot, X., Gasparrini, M., Gerdes, A., Bonifacie, M., Rouchon, V., 2018. An emerging
- thermochronometer for carbonate-bearing rocks:  $\Delta_{47}/(\text{U-Pb})$ . Geology 46(12), 1067-1070.
- McNamara, D., Walter, W., Owens, T., Ammon, C., 1997. Upper mantle velocity structure beneath
- the Tibetan Plateau from Pn travel time tomography. J. Geophys. Res. 102(B1), 493-505.

- Molnar, P., Boos, W.R., Battisti, D.S., 2010. Orographic controls on climate and paleoclimate of
- Asia: Thermal and mechanical roles for the Tibetan Plateau. Annu. Rev. Earth Planet. Sci.
- 860 38, 77-102.
- Mueller, M., Igbokwe, O.A., Walter, B., Pederson, C.L., Riechelmann, S., Richter, D.K., Albert,
- R., Gerdes, A., Buhl, D., Neuser, R.D., Bertotti, G., Immenhauser, A., 2020. Testing the
- preservation potential of early diagenetic dolomites as geochemical archives. Sedimentology
- 864 67(2), 849-881.
- Mueller, M., Walter, B.F., Swart, P.K., Jöns, N., Jacquemyn, C., Igbokwe, O.A., Immenhauser,
- A., 2022. A tale of three fluids: Fluid-inclusion and carbonate clumped-isotope
- paleothermometry reveals complex dolomitization and dedolomitization history of the
- latemar platform. J. Sediment. Res. 92(12), 1141-1168.
- Nooitgedacht, C., van der Lubbe, H., Ziegler, M., Staudigel, P., 2021. Internal water facilitates
- thermal resetting of clumped isotopes in biogenic aragonite. Geochem. Geophys. Geosyst.
- 871 22(5), e2021GC009730.
- Nuriel, P., Wotzlaw, J.F., Ovtcharova, M., Vaks, A., Stremtan, C., Šala, M., Roberts, N.M.W.,
- Kylander-Clark, A.R.C., 2021. The use of ash-15 flowstone as a matrix-matched reference
- material for laser-ablation U-Pb geochronology of calcite. Geochronology 3(1), 35-47.
- Pagel, M., Bonifacie, M., Schneider, D.A., Gautheron, C., Brigaud, B., Calmels, D., Cros, A.,
- 876 Saint-Bezar, B., Landrein, P., Sutcliffe, C., Davis, D., Chaduteau, C., 2018. Improving
- paleohydrological and diagenetic reconstructions in calcite veins and breccia of a
- sedimentary basin by combining  $\Delta_{47}$  temperature,  $\delta^{18}O_{\text{water}}$  and U-Pb age. Chem. Geol. 481,
- 879 1-17.
- 880 Passey, B.H., Henkes, G.A., 2012. Carbonate clumped isotope bond reordering and
- geospeedometry. Earth Planet. Sci. Lett. 351, 223-236.
- Paton, C., Hellstrom, J., Paul, B., Woodhead, J., Hergt, J., 2011. Iolite: Freeware for the
- visualisation and processing of mass spectrometric data. J. Anal. At. Spectrom. 26(12), 2508-
- 884 2518.
- Perez-Beltran, S., Zaheer, W., Sun, Z., Defliese, W.F., Banerjee, S., Grossman, E.L., 2023. Density
- functional theory and ab initio molecular dynamics reveal atomistic mechanisms for
- carbonate clumped isotope reordering. Sci. Adv. 9(26), eadf1701.
- Pettke, T., Oberli, F., Audétat, A., Guillong, M., Simon, A.C., Hanley, J.J., Klemm, L.M., 2012.
- Recent developments in element concentration and isotope ratio analysis of individual fluid
- inclusions by laser ablation single and multiple collector icp-ms. Ore Geol. Rev. 44, 10-38.
- Quade, J., Leary, R., Dettinger, M.P., Orme, D., Krupa, A., DeCelles, P.G., Kano, A., Kato, H.,
- Waldrip, R., Huang, W., Kapp, P., 2020. Resetting southern Tibet: The serious challenge of
- obtaining primary records of paleoaltimetry. Global Planet. Change 191, 103194.

- Raymo, M., Ruddiman, W.F., 1992. Tectonic forcing of late Cenozoic climate. Nature 359(6391), 117-122.
- 896 Roberts, N.M.W., Drost, K., Horstwood, M.S.A., Condon, D.J., Chew, D., Drake, H., Milodowski,
- A.E., McLean, N.M., Smye, A.J., Walker, R.J., Haslam, R., Hodson, K., Imber, J., Beaudoin,
- N., Lee, J.K., 2020. Laser ablation inductively coupled plasma mass spectrometry (LA-ICP-
- MS) U-Pb carbonate geochronology: Strategies, progress, and limitations. Geochronology
- 900 2(1), 33-61.
- 901 Roberts, N.M.W., Rasbury, E.T., Parrish, R.R., Smith, C.J., Horstwood, M.S.A., Condon, D.J.,
- 902 2017. A calcite reference material for LA-ICP-MS U-Pb geochronology. Geochem. Geophys.
- 903 Geosyst. 18(7), 2807-2814.
- Rowley, D.B., Currie, B.S., 2006. Palaeo-altimetry of the late Eocene to Miocene Lunpola Basin, central Tibet. Nature 439(7077), 677-681.
- Rowley, D.B., Garzione, C.N., 2007. Stable isotope-based paleoaltimetry. Annu. Rev. Earth Planet. Sci. 35, 463-508.
- Ryb, U., Lloyd, M.K., Eiler, J.M., 2021. Carbonate clumped isotope constraints on burial, uplift, and exhumation histories of the Colorado Plateau. Earth Planet. Sci. Lett. 566, 116964.
- 910 Shenton, B.J., Grossman, E.L., Passey, B.H., Henkes, G.A., Becker, T.P., Laya, J.C., Perez-Huerta,
- A., Becker, S.P., Lawson, M., 2015. Clumped isotope thermometry in deeply buried
- sedimentary carbonates: The effects of bond reordering and recrystallization. Geol. Soc. Am.
- 913 Bull. 127(7-8), 1036-1051.
- 914 Smedley, P., Kinniburgh, D., 2023. Uranium in natural waters and the environment: Distribution, speciation and impact. Appl. Geochem., 105534.
- Spicer, R.A., Farnsworth, A., Su, T., 2020. Cenozoic topography, monsoons and biodiversity conservation within the Tibetan region: An evolving story. Plant Divers. 42(4), 229-254.
- 918 Stolper, D.A., Eiler, J.M., 2015. The kinetics of solid-state isotope-exchange reactions for clumped
- 919 isotopes: A study of inorganic calcites and apatites from natural and experimental samples.
- 920 Am. J. Sci. 315(5), 363-411.
- 921 Sun, J., Li, J., Liu, W., Windley, B.F., Farnsworth, A., Jin, C., Zhang, Z., Xiao, W., 2022. Middle
- Miocene paleoenvironmental change and paleoelevation of the Lunpola Basin, central Tibet.
- 923 Global Planet. Change 220, 104009.
- 924 Sun, Z., Perez-Beltran, S., Zaheer, W., Defliese, W.F., Banerjee, S., Grossman, E.L., 2023.
- 925 Clumped isotope reordering kinetics in strontianite and witherite: Experiments and first-
- principles simulations. Earth Planet. Sci. Lett. 624, 118467.
- 927 Swart, P.K., 2015. The geochemistry of carbonate diagenesis: The past, present and future.
- 928 Sedimentology 62, 1233-1304.

- Tucker, M.E., 1990. Diagenetic processes, products and environments, in: Tucker, M.E., Wright, V.P. (Eds.), Carbonate Sedimentology. Blackwell, pp. 314-364.
- Vasconcelos, C., McKenzie, J.A., Bernasconi, S., Grujic, D., Tiens, A.J., 1995. Microbial
- mediation as a possible mechanism for natural dolomite formation at low temperatures.
- 933 Nature 377(6546), 220-222.
- 934 Veillard, C.M.A., John, C.M., Krevor, S., Najorka, J., 2019. Rock-buffered recrystallization of
- Marion Plateau dolomites at low temperature evidenced by clumped isotope thermometry
- and X-ray diffraction analysis. Geochim. Cosmochim. Acta 252, 190-212.
- Wang, Z., Nelson, D.D., Dettman, D.L., McManus, J.B., Quade, J., Huntington, K.W., Schauer,
- 938 A.J., Sakai, S., 2020. Rapid and precise analysis of carbon dioxide clumped isotopic
- composition by tunable infrared laser differential spectroscopy. Anal. Chem. 92(2), 2034-
- 940 2042.
- Warren, J., 2000. Dolomite: Occurrence, evolution and economically important associations.
- 942 Earth-Sci. Rev. 52(1-3), 1-81.
- Waseem, A., Ullah, H., Rauf, M.K., Ahmad, I., 2015. Distribution of natural uranium in surface
- and groundwater resources: A review. Crit. Rev. Environ. Sci. Technol. 45(22), 2391-2423.
- Winkelstern, I.Z., Lohmann, K.C., 2016. Shallow burial alteration of dolomite and limestone clumped isotope geochemistry. Geology 44(6), 467-470.
- Wu, F.L., Fang, X.M., Yang, Y.B., Dupont-Nivet, G., Nie, J.S., Fluteau, F., Zhang, T., Han, W.X.,
- 948 2022. Reorganization of Asian climate in relation to Tibetan Plateau uplift. Nat. Rev. Earth
- 949 Environ. 3, 684-700.
- Yiong, Z.Y., Liu, X.H., Ding, L., Farnsworth, A., Spicer, R.A., Xu, Q., Valdes, P., He, S.L., Zeng,
- D., Wang, C., Li, Z.Y., Guo, X.D., Su, T., Zhao, C.Y., Wang, H.Q., Yue, Y.H., 2022. The
- rise and demise of the Paleogene central Tibetan valley. Sci. Adv. 8(6), eabj0944.
- 953 Yanay, N., Wang, Z., Dettman, D.L., Quade, J., Huntington, K., Schauer, A., Nelson, D.D.,
- 954 McManus, B., Thirumalai, K., Sakai, S., Morillo, A.R., Mallik, A., 2022. Rapid and precise
- measurement of carbonate clumped isotopes using laser spectroscopy. Sci. Adv. 8(43),
- 956 eabq0611.
- Yin, A., Harrison, T.M., 2000. Geologic evolution of the Himalayan-Tibetan orogen. Annu. Rev.
- 958 Earth Planet. Sci. 28(1), 211-280.

959

#### 961 Figure captions Figure 1. Geologic background. (A) Shaded relief map of the south-central Tibetan Plateau. 962 963 Dashed lines are suture zones; solid lines with barbs are thrust faults. The white box shows the 964 location of the southern Nima Basin in Fig. 1B. Explanations of abbreviations are embedded in B. 965 (B) Simplified geologic map of the southern Nima Basin, showing sedimentary sections (1DC, 966 4DC) and tuff zircon U-Pb ages of DeCelles et al. (2007b). Adapted from Kapp et al. (2007). (C) 967 Simplified stratigraphy of the 4DC section, showing stratigraphic heights of analyzed samples. 968 Adapted from DeCelles et al. (2007b). Open circles on the right indicate carbonate samples and 969 their stratigraphic heights. Note that the majority of samples are lacustrine micrites, except 4DC16 970 (soil carbonate). The letter "V" denotes vein calcite samples. 971 972 Figure 2. Macro- and micro-textures of analyzed carbonate samples. (A) field outcrops showing 973 lacustrine micrite interlayered with massive red siltstones. (B) A micritic carbonate hand sample 974 with vein calcite (4DC41B). (C-F) Petrographic microscope images of representative samples 975 under cross-polarized light. (G-H) SEM images of samples 4DC41B and 4DC51, respectively. 976 EPMA maps of sample 4DC41A (I–J) and 4DC47.2 (K–L) for Ca and Mg elements, respectively. 977 The color bar indicates counts of Ca or Mg element: the red color indicates high counts (high 978 content), and the black color indicates 0 count. 979 980 Figure 3. Carbonate $\delta^{13}C_{carb}$ (VPDB) and $\delta^{18}O_{carb}$ (VPDB) results. (A) The dolomite ratio of representative samples. The dolomite ratio is calculated as dolomite/(dolomite+calcite) (wt%); (B) 981 $\delta^{13}C_{carb}$ vs. $\delta^{18}O_{carb}$ relationship; (C) $\delta^{18}O_{carb}$ values vs. stratigraphic heights of micrite; (D) $\delta^{13}C_{carb}$ 982 values vs. stratigraphic heights of micrite; (E) $\delta^{18}O_{carb}$ values vs. stratigraphic heights of vein 983 984 calcite; (F) $\delta^{13}C_{carb}$ values vs. stratigraphic heights of vein calcite. The two micritic calcite samples 985 (4DC51 and 4DC64) are marked with gray ovals. 986 987 **Figure 4.** Measured and calculated clumped isotope temperatures of different types of carbonates. 988 The green arrows point to pure calcite samples. 989 990 991

**Figure 5.** Model results of solid-state bond reordering of both calcite (A–B) and dolomite (C–D) using the HH21 model (Hemingway and Henkes, 2021). Solid thick and dotted thin lines are the mean and 95% confidence of forward modeled data; dashed thick lines are equilibrium values. Also labeled are the initial and final clumped isotope temperatures of carbonate, as well as maximum burial temperatures. All simulations are of the same burial and exhumation scenarios: 25–20 Ma gradual burial, 20–10 Ma deep burial to different maximum temperatures (differentiated by different colors, i.e., blue, orange, and black), and 10–0 Ma exhumation to surface. See Supplementary Table S2 for results of all modeling runs.

998

992

993

994

995

996

999	Figure 6. Model results of solid-state bond reordering of calcite using different models: (A) HH21
1000	(Hemingway and Henkes, 2021), (B) Heal4 (Henkes et al., 2014), and (C) SE15 (Stolper and
1001	Eiler, 2015) models.
1002	
1003	Figure 7. Carbonate U and Th content (ppm) analyzed using the LA-ICPMS method. Note the
1004	changing scale of the U content. The inset shows an enlarged area for the 0-1 ppm range of U.
1005	
1006	Figure 8. Proposed carbonate diagenetic history for the 4DC section of the Nima Basin. The thick
1007	black arrow indicates sequential burial/diagenetic history. Limestone was deposited in the Nima
1008	Lake at 26-25 Ma (T0); later, when the section was shallowly buried at 34-40 °C, partial
1009	dolomitization occurred in fluid that is likely different from surface water (T1); further burial to a
1010	depth of 120–130 °C temperatures (T2) caused the formation of high-temperature vein calcite;
1011	solid-state bond reordering of the micritic calcite that is unaffected by thermal fluid to 50–60 °C;
1012	open-system recrystallization of the calcite component of micrites that are close to thermal fluid
1013	to record 100–130 °C temperatures, while the associated dolomite component experienced neither
1014	open-system recrystallization nor significant solid-state bond reordering. See text for more details.

1015

 Table 1. Summary of XRD results.

Sample ID	Dolomite (wt%)	Calcite (wt%)	Quartz (wt%)	Others (wt%)	Dolomite+Calcite (wt%)	Dolomite ratio*
4DC16 <sup>†,#</sup>	0	88	12	0	88	0
4DC34	64	17	16	3	81	79
4DC47	56	17	24	3	73	77
4DC41B	55	28	15	2	83	66
4DC47.2	53	26	17	4	79	67
4DC51#	0	91	6	3	91	0
4DC64#	1	44	43	12	45	2
4DC105	54	35	8	3	89	61
4DC112	70	6	19	5	76	93

Note: wt% indicates weight percentage.

1016

1017

<sup>\*</sup>dolomite ratio is defined as dolomite/(dolomite+calcite).

<sup>†</sup> Note that 4DC16 is a paleosol carbonate sample, while all others are lacustrine micrite.

<sup>\*</sup> Note that these three samples have distinctly low to no dolomite content compared to other samples.

 Table 2. Summary of carbonate clumped isotope data#.

Sample name	Rep.	δ <sup>13</sup> C <sub>carb</sub> (VPDB	SD (‰)	δ <sup>18</sup> O <sub>carb</sub> (VPDB	SD (‰)	Δ638 <sub>CDES</sub> (‰)*	SD (‰)	1 SE (‰)	95% conf.	Temp.^ (°C)	error <sup>¶</sup> (°C)	$\delta^{18}O_{w}$ (VSMOW /%)	Error (‰)
Micrite													
4DC16§	5	-3.82	0.03	-16.86	0.04	0.592	0.018	0.004	0.007	41.0	3.1	-11.75‡	0.69
4DC34	5	-5.02	0.01	-12.89	0.02	0.580	0.011	0.004	0.007	45.5	3.2	-6.95‡	0.69
4DC41B-1	4	-2.86	0.02	-11.68	0.04	0.549	0.004	0.004	0.007	58.8	3.8	-3.47‡	0.73
4DC41B-2	4	-2.60	0.01	-11.66	0.04	0.540	0.012	0.004	0.008	62.8	4.0	-2.81‡	0.74
4DC47.2	4	-0.89	0.01	-9.22	0.02	0.559	0.014	0.004	0.008	54.4	3.8	-1.72‡	0.75
4DC51	5	-0.44	0.03	-16.78	0.02	0.550	0.013	0.002	0.004	58.1	2.5	-8.72‡	0.56
4DC64	5	-1.65	0.14	-17.40	0.31	0.571	0.017	0.002	0.004	49.4	2.3	-10.80‡	0.56
4DC112	4	-1.13	0.02	-12.85	0.00	0.593	0.012	0.004	0.007	40.7	3.3	-7.76‡	0.71

<u>Vein calci</u>	<u>te</u>												
4DC41B-	V 4	-2.63	0.01	-18.52	0.02	0.445	0.005	0.004	0.008	118.1	6.5	-2.17	0.84
Nima10-V	4	-0.57	0.02	-18.41	0.03	0.437	0.014	0.004	0.008	124.1	7.0	-1.37	0.88
Nima11-V	4	-0.73	0.02	-18.12	0.03	0.441	0.017	0.004	0.008	121.0	6.8	-1.43	0.87
<u>Dolomite</u>	only†												
4DC34-D3	1 4	-4.96	0.01	-12.68	0.03	0.610	0.004	0.003	0.007	34.4	2.9	-11.37	0.68
4DC34-D2	2 4	-4.81	0.04	-12.31	0.03	0.593	0.013	0.004	0.007	40.7	3.1	-9.86	0.69
4DC41B- D1	5	-2.61	0.02	-9.73	0.03	0.595	0.024	0.004	0.007	40.0	3.2	-7.40	0.71
4DC41B- D2	5	-2.60	0.01	-9.57	0.03	0.585	0.014	0.004	0.007	43.7	3.3	-6.60	0.71

Note: Rep. no., replicate number; SD, standard deviation; SE, standard error; 95% conf., 95% confidence interval; Temp., temperature.

<sup>\*</sup> See Supplementary Data S1 for the full data set, including removed outliers; Supplementary Data S2 for data of all standards.

<sup>\*</sup> In the new TILDAS system,  $\Delta_{638}$  is equivalent to the conventional  $\Delta_{47}$ . See method section 3.3 for more information.

<sup>^</sup> The temperature calibration equation is:  $\Delta 638_{\text{CDES}} = 0.0409 \pm 0.0003 \times (10^6/\text{T}^2) + 0.1776 \pm 0.0031$ ,  $R^2 = 0.997$  (Yanay et al., 2022).

- The temperature error is calculated using the "pooled" standardization approach of Daëron (2021).
- <sup>‡</sup> Note that although the stable isotope values of paleo-fluids of these samples were provided, we emphasize that these measured bulk samples contain a calcite component that experienced open-system recrystallization or solid-state bond reordering, and thus records elevated temperatures, and as a result, the calculated water isotopes are meaningless.
- § 4DC16 is a soil carbonate, and all the others are lacustrine carbonates.

1020

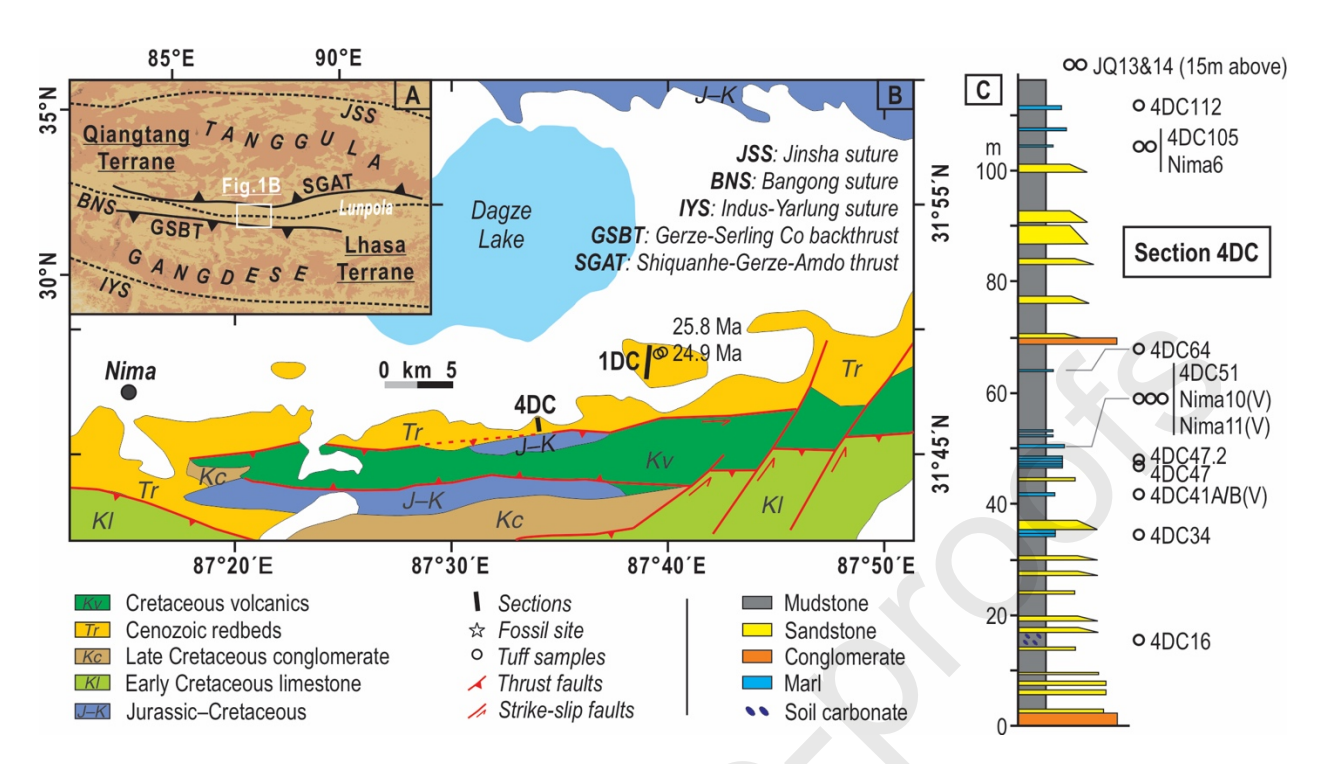
† D1 indicates micrites reacted with acetic acid for 60 minutes, while D2 indicates a reaction time of 120 minutes.

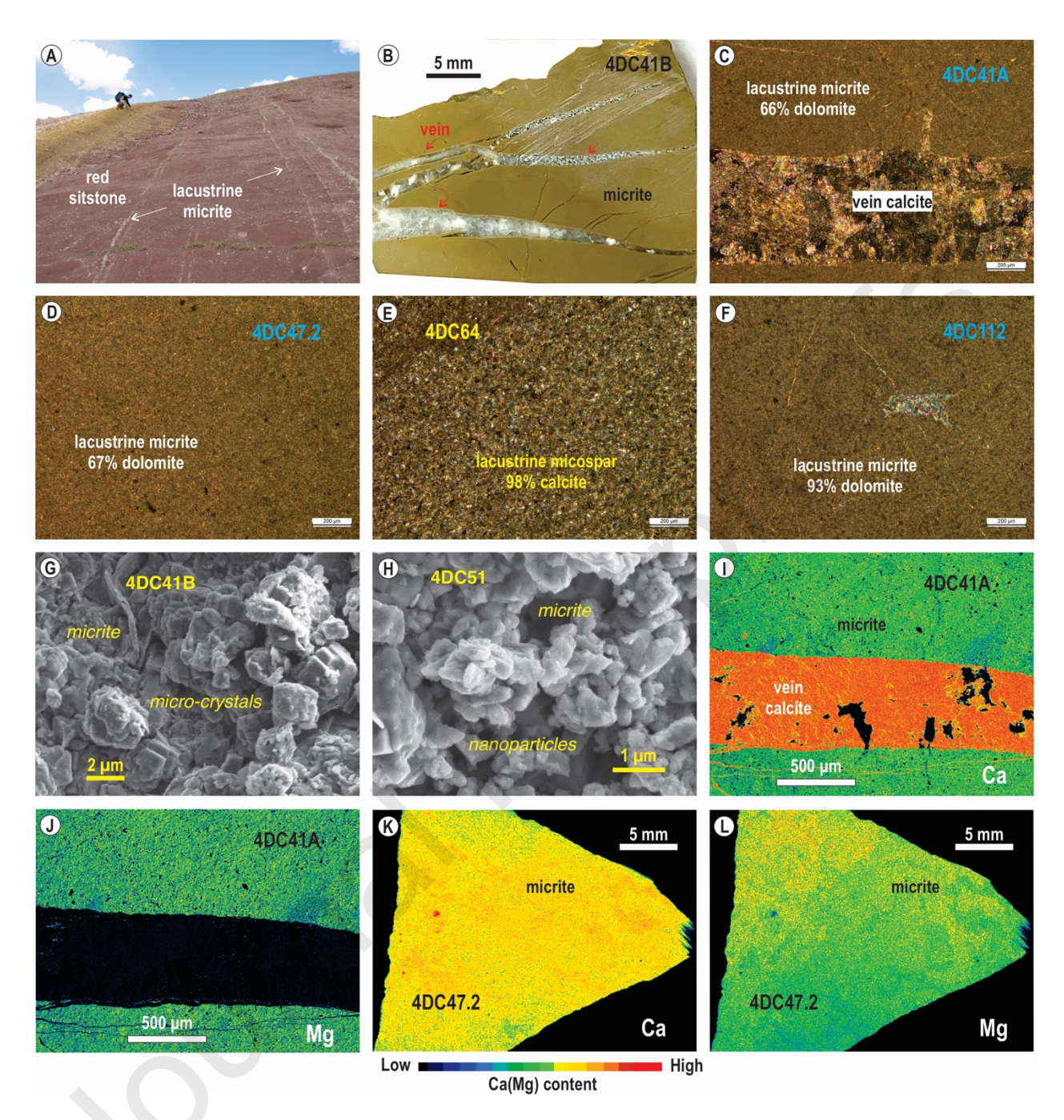
Table 3. Summary of the diagenetic history and changes in mineralogy, stable and clumped isotopes.

Stages*	Settings	Deposition/ diagenesis	$\delta^{18} O_{carb}$ values	Clumped isotope temperatures
Т0	Earth-surface (20–30 °C)	Primary deposition of limestone	Record those of lake water	Record those of lake water
T1	Shallow burial at 34– 40 °C depth	Partial dolomitization	<ul> <li>Newly formed dolomite component records those of basinal fluid</li> <li>Remaining calcite component records those of surface lake water</li> </ul>	<ul> <li>Newly formed dolomite component records elevated burial temperatures of 34–40°C</li> <li>Remaining calcite component records surface lake water temperatures</li> </ul>
T2	Deep burial at ~120–130 °C depth	Solid-state bond reordering, open- system recrystallization, and precipitation of vein calcite	<ul> <li>Vein calcites record those of thermal fluid</li> <li>No stable isotope changes to the few micritic calcite samples<sup>†</sup></li> <li>The stable isotopes of the calcite component record those of thermal fluid<sup>†</sup></li> <li>No stable isotope changes to the dolomite component</li> </ul>	<ul> <li>Vein calcites record high temperatures of thermal fluid (120–130°C)</li> <li>The few micritic calcites experienced bond reordering to 50–60 °C temperatures†</li> <li>The calcite component experienced opensystem recrystallization to record 100–130 °C temperatures†</li> <li>The dolomite component experienced neither open-system recrystallization nor significant solid-state reordering (i.e. only ~1 °C increase)</li> </ul>

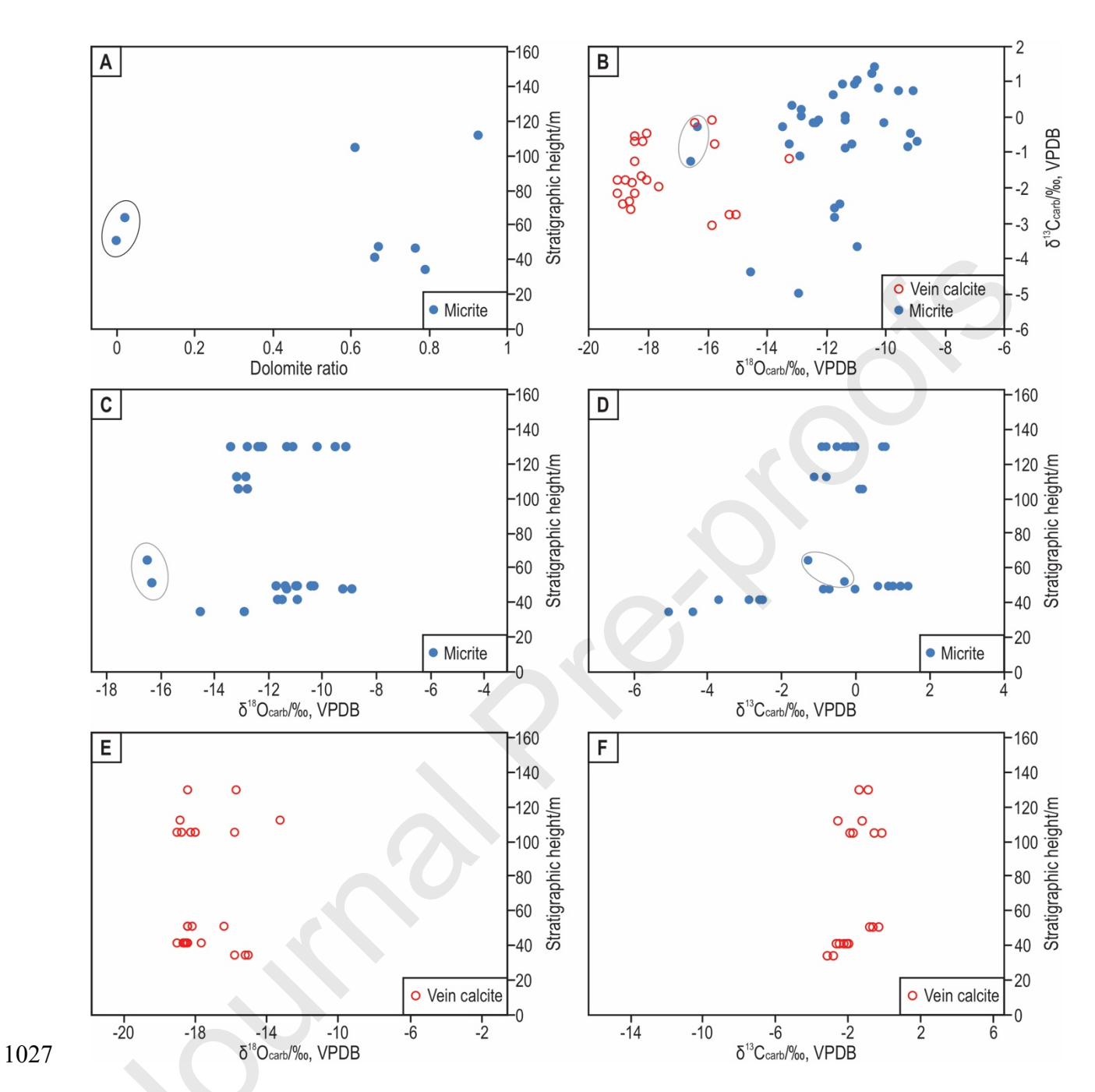
<sup>\*</sup> The T0-T2 stages (from old to young) correspond to those in Fig. 8.

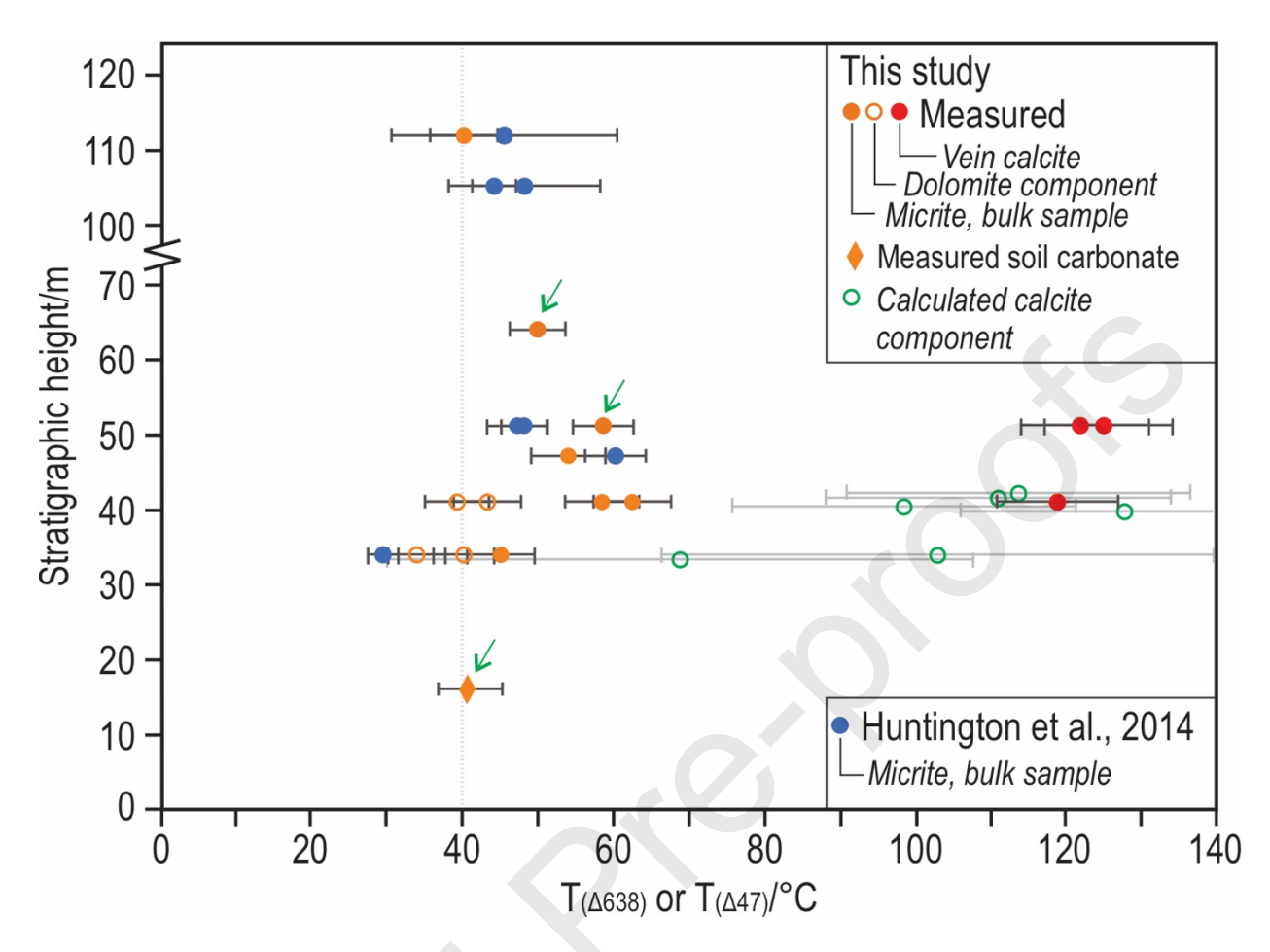
<sup>†</sup> The different behaviors between the micritic calcite (e.g., 4DC51 and 4DC64) and the calcite component (e.g., 4DC34 and 4DC41B) are probably due to the fact that the former is far away from and unaffected by thermal fluid, and the latter is adjacent to and influenced by thermal fluid.

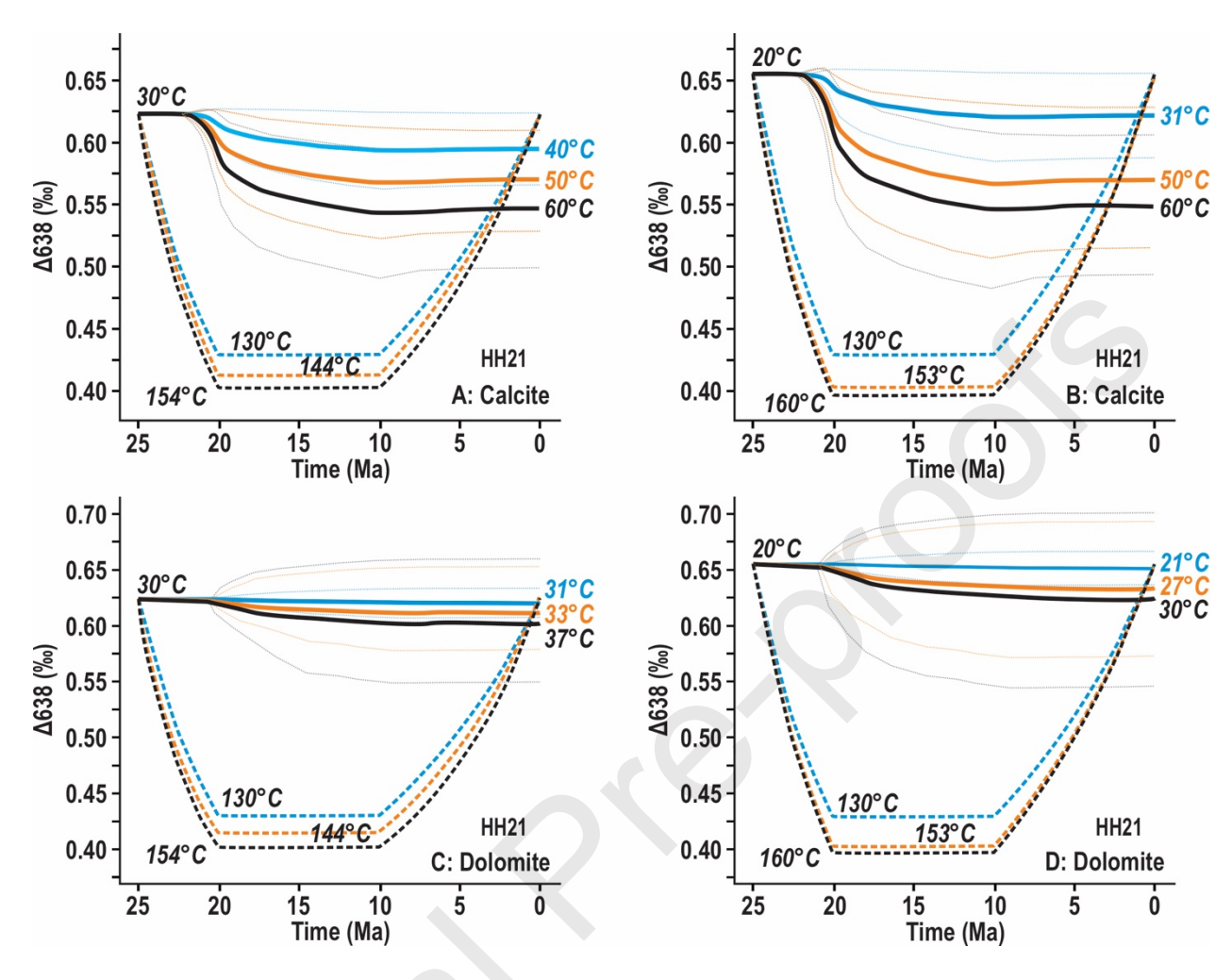


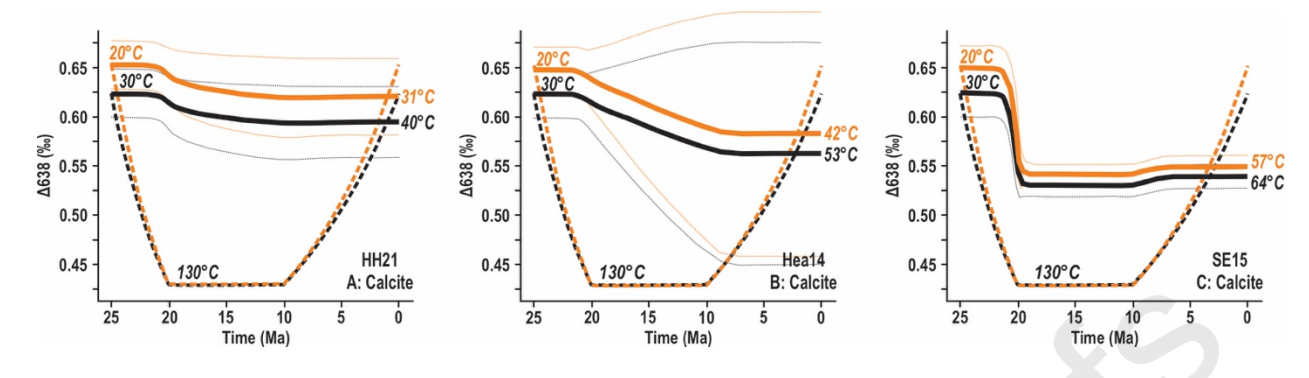


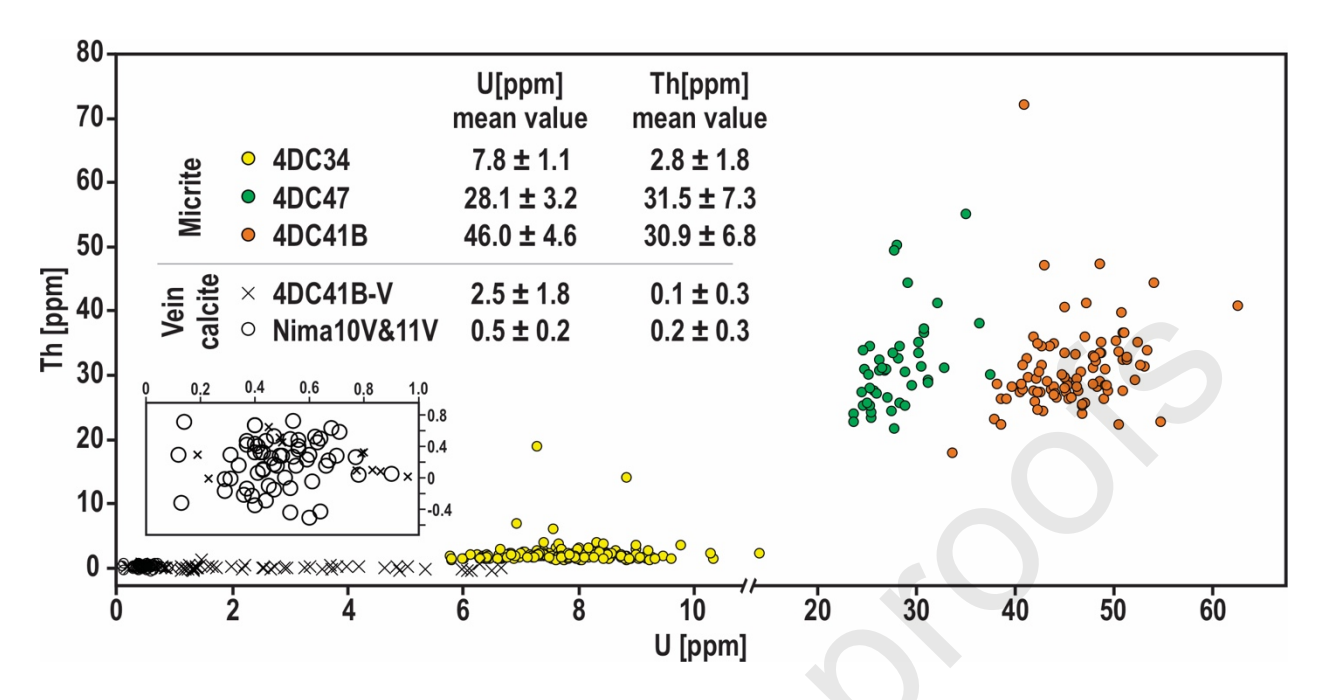
1026 Figure 2

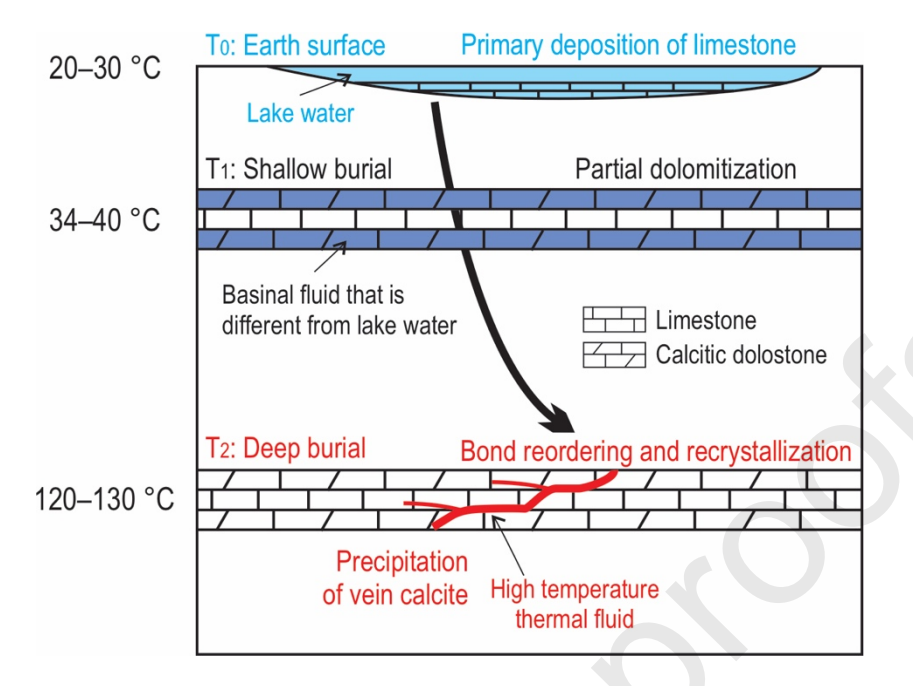












# 1038 Figure 8

